LAWRENCE
LIVERMORE
NATIONAL
LABORATORY

LLNL-JRNL-474853

Comprehensive chemical kinetic modeling of the oxidation of C8 and larger n-alkanes and 2-methylalkanes

S. M. Sarathy, C. K. Westbrook, W. J. Pitz, M. Mehl, C. Togbe, P. Dagaut, H. Wang, M. Oehlschlaeger, U. NIemann, K. Seshadri, P. S. Veloo, C. Ji, F. Egolfopoulos, T. Lu

March 21, 2011

Combustion and Flame

Disclaimer

Comprehensive chemical kinetic modeling of the oxidation of C_8 and larger *n*-alkanes and *2*-methylalkanes

S.M. Sarathy[1*], C.K. Westbrook[1], M. Mehl[1], W.J. Pitz[1]

C. Togbe[2], P. Dagaut[2]

H. Wang[3], M.A. Oehlschlaeger[3]

U. Niemann[4], K. Seshadri[4]

P.S. Veloo[5], C. Ji[5], F. Egolfopoulos[5]

T. Lu[6]

[1] *Lawrence Livermore National Laboratory, Livermore, California, USA*

[2] *CNRS Orleans, France*

[3] *Rensselaer Polytechnic Institute, Troy, New York, USA*

[4] *University of California, San Diego, California USA*

[5] *University of Southern California, Los Angeles California, USA*

[6] *University of Connecticut, Storrs, Connecticut, USA*

**** Corresponding author***

sarathy1@llnl.gov

925.423.6011

Conventional petroleum jet and diesel fuels, as well as alternative Fischer-Tropsch (FT) fuels and hydrotreated renewable jet (HRJ) fuels, contain high molecular weight lightly branched alkanes (i.e., methylalkanes) and straight chain alkanes (*n*-alkanes). Improving the combustion of these fuels in practical applications requires a fundamental understanding of large hydrocarbon combustion chemistry. This research project presents a detailed and reduced chemical kinetic mechanism for singly methylated iso-alkanes (i.e., 2-methylalkanes) ranging from C_8 to C_{20}. The mechanism also includes an updated version of our previously published C_8 to C_{16} *n*-alkanes model. The complete detailed mechanism contains approximately 7,200 species 31,400 reactions. The proposed model is validated against new experimental data from a variety of fundamental combustion devices including premixed and non-premixed flames, perfectly stirred reactors and shock tubes. This new model is used to show how the presence of a methyl branch affects important combustion properties such as laminar flame propagation, ignition, and species formation.

Keywords: combustion, iso-alkanes,n-alkanes, 2-methylalkanes, detailed chemical kinetic modeling, autoignition, perfectly stirred reactor, counterflow diffusion flame, premixed laminar flame speed, mechanism reduction, surrogate fuel models

1.0 Introduction

Detailed chemical kinetic combustion models of real fuels (e.g., gasoline, diesel, and jet fuels) are important tools for improving the design, efficiency, and environmental performance of combustion technologies. Fuels derived from conventional petroleum feedstock often are comprised of thousands of different hydrocarbon compounds. This complexity makes it challenging to develop detailed chemical kinetic models of real fuels because modeling each fuel component would be computationally expensive. One way of reducing complexity is to group fuel compounds together into structural classes, and formulate a smaller "surrogate fuel" model that represents the chemical and physical characteristics of the real fuel. In this way the chemical kinetic model becomes easier to build and less computationally expensive to solve in a reacting flow simulation.

Previous studies at the Lawrence Livermore National Laboratory have presented detailed chemical kinetic models for several important structural classes found in real fuels, such as *n*-alkanes [1,2], *iso*-alkanes [3,4,5,6], alkenes [7,8], aromatics [10], and cyclo-alkanes [11,12]. Surrogate fuel models have also been developed for gasoline fuel [10,13] and gasoline and diesel primary reference fuels [14] by merging the models of relevant structural classes. A recent review paper by Pitz and Mueller [15] describes the development of diesel surrogate fuel models. The composition of typical diesel fuels is presented as a mixture of high molecular weight (i.e., C_{10}-C_{20}) *n*-alkanes, lightly branched *iso*-alkanes with one or two methyl groups, cycloalkanes with multiple alkyl side chains, and aromatics with multiple side chains. The recent progress in combustion modeling of these structural classes is discussed in detail; however, the authors conclude that major research gaps remain in modeling high molecular weight (i.e., greater than C_{10}) aromatics, alkyl aromatics, cyclo-alkanes, and lightly branched *iso*-alkanes.

The focus of the present research study is on high molecular weight *2*-methylalkanes from C_8 to C_{20}. *n*-Alkyl radicals are an important intermediate in the combustion of *2*-methylalkanes, so this study also presents an updated version of our previously published C_8-C_{16} *n*-alkanes model [2]. *2*-methylalkane and *n*-alkane structures are important components of conventional diesel fuels derived from petroleum [15,16], synthetic Fischer-Tropsch diesel and jet fuels derived coal, natural gas, and/or biomass [17,18], and renewable diesel and jet fuels derived from thermochemical treatment of bio-derived fats and oils (e.g., hydrotreated renewable jet (HRJ) fuels) [19]. Significant effort is placed on understanding the effect of carbon chain length and methyl substitution along the chain on important combustion properties.

1.1 Previous Combustion Studies on 2-methylalknes

Limited research has been performed on the fundamental combustion properties of *2*-methylalkanes. *iso*-Butane (*2*-methylpropane, iC_4H_{10}) has been studied in engines Wilk et al. [20] and in shock tubes by Ogura et al. [21], Oehlschlaeger et al. [22], and Healy et al. [23]. Burcat et al. [24] studied

the high temperature shock tube autoignition of 2-methylpentane (C_6H_{14}-2). Several experimental and kinetic modeling studies have been performed on 2-methylhexane (C_7H_{16}-2) by Westbrook et al. [5,6], Griffiths et al. [25], and Silke et al. [26]. 2-methylheptane (C_8H_{18}-2) has been studied by Kahandwala et al. [27] in high temperature shock tubes. Sarathy et al. [28] recently presented a high temperature chemical kinetic model for 2-methylheptane and validated it against counterflow diffusion flame species profiles. In summary, the aforementioned studies conclude the *2*-methylalkanes are less reactive under autoignition conditions than *n*-alkanes of the same chain length. At lower temperatures, the decreased reactivity is attributed to depressed of RO_2 isomerization reactions in the branched alkane; and at high temperatures, the branch alkanes are less reactive since they lead to the unreactive resonantly stabilized allyl (C_3H_5) radical via propene (C_3H_6) [21]. The flame studies reveal indicated that *2*-methylalkanes produce more branched alkenes (i.e., *2*-methylalkenes) and propene due to the presence of a tertiary C-H bond [28].

1.2 Ignition Quality of 2-methylalkanes

A fuel's autoignition properties are typically quantified using the familiar octane and cetane scales. In both scales, an *n*-alkane is used as a reference compound for the most easily ignited fuel (i.e., *n*-heptane and *n*-hexadecane), while a highly branched alkane is used as reference compound for the least easily ignited fuel (i.e., *iso*-octane and *2,2,4,4,6,8,8*-heptylmethylnonane). The high ignition quality of *n*-alkanes is attributed to their low temperature reactivity, which leads to degenerate chain branching and early heat release. On the other hand, the poor ignition quality of highly branched alkanes is due to the inability of these compounds to lead to degenerate chain branching under low temperature oxidation conditions.

One goal of the present study is to elucidate the effects of methyl branching on the autoignition properties of *2*-methylalkanes by comparing their reactivity with *n*-alkanes of the same chain length. A simple and practical method of comparing the ignition quality of two fuels is to compare their derived cetane numbers (DCN) using the ASTM 6890 method [29] in an ignition quality tester (IQT) [30,31].

Table 1 presents unpublished NREL IQT test data for two *n*-alkanes (i.e., *n*-heptane and *n*-octane) and their *2*-methylalkane counterparts (i.e., *2*-methylhexane and *2*-methylheptane). The results indicate that *2*-methylalkanes are slower to ignite than *n*-alkanes of the same chain length. These results are consistent with the general understanding that alkane branching decreases the ignition quality of a fuel. The present study will attempt to further clarify the differences in autoignition quality of *n*-octane versus *2*-methylheptane using fundamental shock tube autoignition data and a detailed chemical kinetic modeling simulations.

2.0 Chemical Kinetic Mechanism Formulation

The proposed detailed chemical kinetic mechanism includes both low-temperature and high-temperature kinetic schemes for *2*-methylalkanes from C_7 to C_{20}. Winclude the important reaction pathways based on the early work of Curran et al. on *n*-heptane and *iso*-octane [1,3]. In addition, we include an updated version of our C_8-C_{16} *n*-alkane sub-mechanism initially developed by Westbrook et al. [2]. The data files for the complete model include a detailed chemical kinetic reaction mechanism, a dataset of thermochemical properties, and a dataset of transport properties. The entire model consists of approximately 7,200 species and 31,400 reactions. These input files are available as supplemental material to this publication and from our website at:
https://www-pls.llnl.gov/?url=science_and_technology-chemistry-combustion.

The "core mechanism" used here is our latest detailed mechanism for *n*-heptane, which was presented and discussed as part of the gasoline surrogates model by Mehl et al. [10,13]. This core mechanism is comprised of an updated C_0-C_5 sub-mechanism [32,33], the C_6-C_7 alkane sub-mechanism from Mehl et al. [10,13], and the C_5-C_7 alkenes sub-mechanism from Mehl et al. [7,8]. We found the following two errors in the C_0-C_5 sub-mechanism that were corrected to obtain converged counter-flow flame simulations:

- The reaction ch2(s)<=>ch2 was changed to ch2(s)+m<=>ch2+m and is consistent with the current bi-molecular rate constant expression.
- The specified reverse rate for the reaction o+c2h2<=>c2h+oh was above the collisional limit at 300 K, so the rate was changed to have an A factor of $9x10^{13}$ with no temperature dependence.

We initiated the present work by building a high-temperature mechanism for the C_8 *2*-methylalkane (i.e., *2*-methylheptane), which was previously discussed by Sarathy et al. [28]. The *2*-methylheptane mechanism was built in a modular fashion, starting with the high temperature reactions (i.e., classes 1-10) for 2-methylhexane described by Westbrook et al. [5,6], and subsequently adding the analogous pathways for 2-methylheptane. This study follows a similar methodology to develop the high-temperature reaction pathways for 2-methylalkanes up to C_{20}. As a result, the mechanism requires high-temperature reaction pathways for *n*-alkyl radicals up to C_{19} as well. The C_8-C_{16} *n*-alkyl species, are already present in the C_8-C_{16} *n*-alkane sub-mechanism from Westbrook et al. [2], so we only add the relevant high-temperature reaction classes (i.e., classes 3-9) for C_{17}-C_{19} *n*-alkyl species.

The low-temperature reaction pathways for *2*-methylalkanes (i.e., classes 11-30) are written starting with those for *2*-methylhexane from Westbrook et al. [2]. The analogous pathways are then written for all *2*-methylalkanes from C_8 to C_{20}. Several modifications are made to the reaction pathways

and reaction rate rules presented in our previous hydrocarbon mechanisms [1-3] to make the proposed mechanism consistent with our recent gasoline surrogates mechanism [10,13] and to better agree with the experimental data presented herein.

2.1 Naming of Species

To illustrate the naming of the species for the *2*-methylalkanes mechanism, *2*-methylheptane is denoted as C_8H_{18}-2 in the mechanism, for example (see Figure 1 for its molecular structure). The carbon chain is labeled numerically (i.e., 1, 2, 3, etc.) such that the location number of the methyl branch is minimized. For *2*-methylheptene species, the location of a double bond is identified by a hyphen followed by the number of the first carbon in the double bond (e.g., *2*-methyl-*3*-heptene is C_8H_{16}-3-2). Additional notations are provided to denote radical sites in the molecule. The carbon sites are labeled alphabetically (i.e., a, b, c, etc.) such that the location of the first methyl branch is minimized (Figure 1). In this way, the 2-methyl-3-heptyl radical is denoted as C_8H_{17}-2c, while the *2*-methyl-1-heptyl radical is written as C_8H_{17}-2a. For larger *2*-methylalkanes, the same naming convention is used with added letters and numbers to account for the additional carbons on the chain. For example, the structure and naming convention of *2*-methyldecane is given in Figure 1.

2.2 Classes of Reactions

The major classes of elementary reactions considered for the oxidation of C_8-C_{16} *n*-alkanes and C_7-C_{20} 2-methylalkanes include the following:

High Temperature Reaction Classes

1. Unimolecular fuel decomposition
2. H-atom abstraction from the fuel
3. Alkyl radical decomposition
4. Alkyl radical isomerization
5. H-atom abstraction reactions from alkenes
6. Addition of radical species O and OH to alkenes
7. Reactions of alkenyl radicals with HO2, CH3O2, and C2H5O2
8. Alkenyl radical decomposition
9. Alkene decomposition
10. Retroene decomposition reactions

Low Temperature Reaction Classes

11. Addition of O_2 to alkyl radicals ($R + O_2 = ROO$)
12. $R + ROO = RO + RO$
13. $R + HO_2 = RO + OH$
14. $R + CH_3O_2 = RO + CH_3O$
15. Alkyl peroxy radical isomerization ($ROO = QOOH$)
16. Concerted eliminations ($ROO = \text{alkene} + HO_2$)
17. $ROO + HO_2 = ROOH + OH$
18. $ROO + H_2O_2 = ROOH + HO_2$
19. $ROO + CH_3O_2 = RO + CH_3O + O_2$
20. $ROO + ROO = RO + RO + O_2$
21. $ROOH = RO + OH$
22. RO decomposition
23. QOOH = cyclic ether + OH (cyclic ether formation via cyclisation of diradical)
24. $QOOH = \text{alkene} + HO_2$ (radical site beta to OOH group)
25. QOOH = alkene + carbonyl + OH (radical site gamma to OOH group)
26. Addition of O_2 to QOOH ($QOOH + O_2 = OOQOOH$)
27. Isomerization of OOQOOH and formation of carbonylhydroperoxide and OH
28. Decomposition of carbonylhydroperoxide to form oxygenated radical species and OH
29. Cyclic ether reactions with OH and HO_2
30. Decomposition of large carbonyl species and carbonyl radicals

2.3 Description of Chemical Kinetic Mechanism

Curran et al. [1,3] have discussed many of the aforementioned reaction classes. For the sake of brevity, this section presents a list summarizing the most notable updates to reaction classes and reaction rate constants in the proposed model. For readers seeking a comprehensive description, we direct them to the supplementary material, where each reaction class, the chosen rate constants, and their sources are described in detail. The most significant model developments are as follows:

- Alkyl radical decomposition (i.e., class 3) and isomerization (i.e., class 4) rates are based on recent kinetic studies at the National Institute of Standards and Technology (NIST) [34-37].
- The reaction rate constants for alkyl peroxy radical isomerization (i.e., class 15) are from our latest *n*-heptane model by Mehl et al. [10]. The rates are originally from Curran et al. [1], but the activation energies are reduced by 400 kcal/mol to follow the recommendations of Zhu et al. [38], and to obtain better agreement in previous work on ignition of *n*-heptane [10].

- We include a new reaction path, not included in our previous *n*-alkanes work [2], of the molecular elimination of HO_2 from ROO (i.e., class 16). This concerted (i.e., direct) elimination of HO_2 from the alkyl peroxy radical (i.e., ROO) occurs via a 5-membered transition state and was first discovered by Quelch et al. [39]. This reaction class was included in our latest *n*-heptane/iso-octane model by Mehl et al. [10] and our cyclohexane model by Silke et al. [39], but we have updated the rate constants in the present study.
- The reaction rate constants for carbonylhydroperoxide decomposition (i.e., class 28) are from our latest *n*-heptane model by Mehl et al. [10]. The activation energy for these reactions was decreased from the work of Curran et al. [1] to better predict low temperature ignition delay times for *n*-heptane [10].

2.4 Thermochemical Data

The thermodymamic parameters for the species are very important because they are used to determine reverse rate constants. The THERM [41] software was used to compute the thermochemical properties of species not present in the *n*-alkane model [2]. The THERM group values are from Benson [42] and Bozzelli [43,44].

2.5 Tranport Properties

Kinetic processes and transport processes are rate controlling in diffusion flames and droplet vaporization/combustion, so transport properties are needed for all the species in the model. This study obtained the molecular transport parameters for species using a variety of methods. The transport properties for species upto C_8 were already available in a previously published *2*-methylheptane model [28]. The transport properties of larger alkanes, alkene, alkyl, and alkenyl species were determined as follows. For stable species, this study used the correlations developed by Tee, Gotoh, and Stewart [45], as described in Holley and coworkers for hydrocarbons [45], to calculate the LJ collision diameter and potential well depth using the critical pressure (P_c), critical temperature (T_c), and boiling point (T_b) of the species. P_c, T_c, and T_b for the majority stable species are based on the recommendations of Owczarek and Blazej [47,48], and the data for missing species was extrapolated. Following previous work [49], the polarizability in cubic Angstroms of stable species was calculated using an empirical correlation [50], which depends on the number of C, H, and O atoms in the molecule. The value calculated using this method were comparable to experimentally measured polarizability for species where such data was available [51]. The dipole moment for all new species was set to zero because all they are non-polar hydrocarbons. The index factor which describes the geometry of the molecule was determined from the molecular structure (i.e., 0 for atoms, 1 for linear molecules, and 2 for nonlinear molecules). We

attempted to calculate different transport properties for alkanes and alkenes of the same chain length according to their differences in corresponding states (e.g., P_c, T_c, and T_b); however, sufficient data was unavailable for large *2*-methylalkenes, so we used the transport parameters of the corresponding *2*-methylalkane. For alkyl and alkenyl radical species, the transport properties of their stable counterpart were used.

We also include a rough estimation of transport properties for species in the low temperature mechanism (i.e., RO, RO2, ROOH, QOOH, cyclic ethers, etc.) by assuming the transport properties are the same as the parent fuel molecule from which they are derived. We acknowledge that this is a poor assumption, but practically we do not expect it to significantly affect simulations since the concentrations of these low temperature species is small and the reactivity of the system is typically dominated by the fuel's transport properties. Nevertheless, we caution researchers interested in using our chemical kinetic model to test the sensitivity of their results on our proposed transport parameters.

3.0 Validation Studies

The proposed model for large *n*-alkanes and *2*-methylalkanes has been validated against a wide range of experimental data . Westbrook et al. [2] previously validated the C_8-C_{16} *n*-alkane mechanism; the present improvements to the reaction classes and rate rules do not significantly alter the validations presented previously. In this study, we include additional new validations for *n*-alkanes, but the focus is on validation data for *2*-methylalkanes. The experimental focus is on *2*-methylheptane since this molecule is easy to work with experimentally (i.e., less expensive and lower boiling point than larger 2-methylalkanes). Validating the mechanism against *2*-methylheptane is considered adequate because the same reaction rate rules are applied for larger *2*-methylalkanes. The following is a list specific validation studies performed:

1. Low and intermediate temperature rapid compression machine (RCM) ignition data for *2*-methylhexane by Silke et al. [26].
2. Jet stirred reactor species profiles data for *2*-methylheptane performed in this study at CNRS, Orleans.
3. Low and high temperature shock tube ignition data for *2*-methylheptane and *n*-octane performed in this study at the Rensselaer Polytechnic University.
4. Kinetic modeling simulations of shock tube ignition delay time for *n*-alkanes and *2*-methylkanes greater than C_8.
5. Premixed laminar flame velocity data for *n*-octane by Ji et al. [53] and Kelley et al. [54] and for *2*-methylheptane performed in this study at the University of Southern California.

6. Counterflow diffusion flame extinction and ignition data for *2*-methylheptane performed in this study by at the University of California San Diego with simulations performed using a skeletal mechanism prepared at the University of Connecticut.

3.1 Rapid Compression Machine (RCM) experiments and simulations for 2-methylhexane

This section uses a detailed chemical kinetic mechanism for *2*-methylhexane to simulate ignition in a RCM. Westbrook et al. [5] and Silke et al. [26,55] present RCM ignition data of *2*-methylhexane in two separate experimental facilities. The present study uses the data obtained by Silke et al. [26,55] to validate the proposed mechanism.

3.1.1 RCM Results

The Galway RCM experiments by Silke et al. [26,55] were obtained at an ϕ=1 (21% O_2, 79% diluent) and an end of compression pressures (Pc) in the range 13.5-15 atm. The initial pressure (Pi), initial temperature (Ti), and diluent gas composition (i.e., concentrations of Ar and N_2) were initially set to achieve the desired Pc and end of compression temperature (Tc). The experiments were conducted at a compression time (tc) of 16.6 ms, and the compression ratio (CR) was in the range 9.5-10.2 depending on the diluent gas composition. The actual Pc was measured for each experimental run, and then Tc was calculated based on ideal gas theory. The ignition delay time (τ_{id}) was defined as the time of maximum pressure rate rise (dP/dt) after the end of compression. Further details of the experimental setup and a raw experimental data are available in Silke's thesis [55].

The present RCM kinetic modeling simulations were performed in CHEMKIN PRO [56] using the homogenous batch reactor code to model the entire compression stroke using the Pi, Ti, CR, and tc. The experimental CR varied slightly with each run, so we assumed a CR of 10 for all simulations. Heat losses in the RCM are usually modeled by using the technique of "heat loss mapping" as described by Dooley et al. [57]; however, a non-reactive pressure trace was not available for conditions similar to the present study (e.g., CR 10), so we were unable to model heat losses after the end of compression. The onset of ignition was determined as the point of maximum temperature rise (max dT/dt), which corresponds closely to the point of maximum pressure rate rise (max dP/dt). The simulated τ_{id} is plotted against the predicted Tc for each simulation run.

The Galway RCM experimental and simulation results are presented in Figure 2. The ignition delay time is plotted against the temperature at the end of compression. The experimentally measured ignition delay times are presented as solid triangles. The simulation data is plotted as a line with open triangles. Overall the model exhibits good agreement in trend with the experimental data. At all temperatures the simulation predicts ignition delay times within two times of the experimental values.

The agreement between simulated and experimental data improves as the temperature increases, and above 750 K there is a very good agreement. Minor negative temperature coefficient behavior is observed in both the experiments and simulations from 750 to 900 K.

3.1 Jet Stirred Reactor (JSR) experiments and simulations for 2-methylheptane

The jet stirred reactor is a fundamental experimental tool for understanding the low temperature and high temperature reactivity of 2-methylheptane, as well as the major and minor species formed at various temperatures and equivalence ratios. The experiments presented herein were conducted at high pressure (i.e., 10 atm) to better study the low temperature reactivity of 2-methylheptane under conditions similar those found in internal combustion engines. This new experimental dataset is used to validate the proposed model and its reaction rate rules used for modeling 2-methylalkanes up to C_{20}.

3.2.1 JSR Experimental Setup

We used the JSR experimental setup utilized in previous studies [58,59]. It consisted of a small spherical fused-silica reactor (4 cm outside diameter) equipped with four nozzles of 1 mm I.D. each. High-purity reactants were used in the present experiments: oxygen (99.995% pure) and 2-methylheptane (>99%). The reactants were diluted with nitrogen (<100 ppm H_2O) and quickly mixed before admission into the injectors. To minimize temperature gradients within the JSR, the reactants were preheated. A Shimadzu LC10 AD VP pump operating with an on-line degasser (Shimadzu DGU-20 A3) was used to distribute the fuel to an in-house atomizer-vaporizer assembly thermally regulated at 473 K. A high degree of dilution (0.15-0.2% mol. of fuel) was used to reduce heat release and temperature gradients inside the JSR. Temperature gradients of ca. 1 K/cm along the vertical axis of the JSR were measured by a 0.1 mm Pt-Pt/Rh-10% thermocouple located inside a thin-wall silica tube to avoid catalytic effects. A movable low-pressure fused silica sonic probe was used to sample the reacting mixtures inside the JSR. The samples were transferred to analyzers via a Teflon heated line (473 K). They were analyzed online by FTIR (cell: 10m path length and 200 mBar; spectral resolution of 0.5 cm-1) and off-line, after collection and storage in 1 L Pyrex bulbs. Gas chromatographs (GC) equipped with capillary columns (DB-624 for oxygenates, CP-Al2O3-KCl for hydrocarbons, and Carboplot-P7 for hydrogen and oxygen), a TCD (thermal conductivity detector), and an FID (flame ionization detector) were used for off-line analyses. Products identification was performed by means of a GC-MS (Varian V1200) operated with electron ionization (70 eV). Fragmentation patterns were compared to data obtained in previous work [60].

The experiments were performed at steady state, at a constant pressure of 10 atm and a constant mean residence time, τ, of 0.7 s. The reactants flowed constantly into the JSR and the temperature of the gases inside the reactor was increased stepwise. A good repeatability of the measurements and a

reasonably good carbon balance (typically 100 ± 10%) were obtained in this series of experiments. Uncertainties for all species concentration measurements were 10% , except for cyclic ether concentration which had a 15% error. Temperature gradients of < 2 K/cm along the vertical axis of the reactor were recorded.

3.2.2 JSR Results

The CHEMKIN PRO [56] transient perfectly stirred reactor code was used to validate the proposed kineic model against jet stirred reactor data for *2*-methylheptane at 10 atm, three equivalence ratios (ϕ= 0.5, ϕ= 1.0, and ϕ= 2.0), and a range of temperatures between 500-1200 K. The JSR allows us to study the oxidation of *2*-methylheptane in a flameless premixed environment. Sonic probe sampling and GC and FTIR analyses measured the concentration of species at each equivalence ratio and temperature condition. The measured species included *2*-methylheptane (C_8H_{16}-2), hydrogen (H_2), oxygen (O_2), water (H_2O), carbon monoxide (CO), carbon dioxide (CO_2), methane (CH_4), acetylene (C_2H_2), ethylene (C_2H_4), ethane (C_2H_6), propene (C_3H_6), ethanal (CH_3CHO), formaldehyde (CH_2O), propanal (C_2H_5CHO), acetone (CH_3COCH_3), *2*-propenal (C_2H_3CHO), *1*-butene (1-C_4H_8), *iso*-butene (iC_4H_8), *1,3*-butadiene (1,3-C_4H_6), butanal (C_3H_7CHO), 2-methyl-5-isopropyl-tetrahydrofuran ($C_8H_{16}O$3-6-2), *5*-ethyl-*2,2*-dimethyl-tetrahydrofuran ($C_8H_{16}O$2-5-2), and *3*-methyl-*5*-propyl-tetrahydrofuran ($C_8H_{16}O$1-4-2).

Figure 3 presents the experimental measurements and modeling results of *2*-methylheptane obtained at ϕ=1.0. The experimental results (symbols) show that with increasing temperature, the *2*-methylheptane concentration drops significantly between 500 K and 650 K. This corresponds to the cool flame reactivity regime, wherein the overall low temperature peroxy sequence is active leading to chain branching. In this region, the first maximum of several oxygenated compounds (e.g., CO, H_2O, CH_2O, acetone, propanal, 2-propenal, and ethanal) is created from the decompositon of ketohydroperoxide species. From 650 K to 750 K, there is an increase in the *2*-methylheptane concentrations exhibiting the negative temperature coefficient (NTC) behavior of the system wherein the concerted elimination reactions and cyclic ether formation are dominant. The cyclic ether species (i.e., furans) reach their peak concentration in this temperature region. Above 750 K, the fuel concentration decreases continuously as low temperature reaction pathways become less important, and high temperature kinetics control the systems reactivity. Many alkene species reach their maximum concentration around 850 K and are then destroyed at higher temperature. 850 K also corresponds to a second maximum in the concentration of small oxygenates, which

The model predictions (open symbols with line) for ϕ=1.0 are also shown in Figure 3. The models ability to reproduce the experimental data is discussed qualitatively and quantitatively. The

model's prediction is considered good if the shape of the model profile closely matches the experimental profile, and if the predicted maximum mole fraction is within a factor 2 of the measured maximum mole fraction. The concentration of the reactants of *2*-methylheptane and O_2 is well predicted at all temperatures, and so is the concentration of the major product species CO, CO_2, and H_2O. The model well predicts the minor species CH_4, H_2, C_2H_2, and C_2-C_8 unsaturated hydrocarbons (i.e., alkenes and dienes). The concentration of oxygenated product species CH_2O and ethanal is well predicted, but 2-propenal is over predicted and butanal is under predicted. The first maximum concentration (i.e, peak) of acetone is well predicted by the model, but the model under predicts the second peak. This discrepancy is related to the formation of acetone from *iso*-butene, which is a reaction sequence that needs further analysis.

The cyclic ether species measured in the JSR are all furans (i.e., 5-membered rings), and the model also predicts that these are the predominant cyclic ether species. This is consistent with the recent findings of Herbinet et al. in their experimental study cyclic ethers formed in the low-temperature oxidation of a series of *n*-alkanes [61]. In the present study, the model well predicts the profiles of the furans; however, the concentration of 2-methyl-5-isopropyl-tetrahydrofuran is over predicted.

Figure 4 and Figure 5 present the experimental and modeling results obtained at ϕ=0.5 and ϕ=2.0 in the JSR, respectively. The experimental data and model predictions show a similar trend as observed at ϕ=1.0. Overall the model predictions are in excellent agreement with the JSR data, especially considering the two studies were conducted separately and not optimized for good agreement.

3.3 Shock Tube Autoignition Experiments and Simulations of *n*-octane and 2-methylheptane

Studying the autoignition of 2-methylalkanes and *n*-alkanes under similar conditions can elucidate the effect fuel molecular structure on low temperature reactivity. It has been shown that 2-methylalkanes have lower cetane numbers than *n*-alkanes of the same chain length. Therefore, the low temperature and negative temperature coefficient (NTC) reactivity of 2-methylalkanes is expected to be lower than *n*-alkanes. Shock tube autoignition studies enable us to study the low temperature and NTC reactivity under idealized conditions. This section presents new experimental data for *n*-octane and 2-methylheptane at 20 atm and a range of equivalence ratios, and uses the data to validate the proposed chemical kinetic model.

3.3.1 Shock Tube Experimental Setup

Ignition delay times were measured for *2*-methylheptane and *n*-octane in reflected shock experiments performed in a heated high-pressure shock tube at Rensselaer Polytechnic Institute. The shock tube has been previously described in detail [62]. The heated shock tube temperature (~100 °C)

was chosen to be sufficiently high to avoid fuel condensation and provide ease of gaseous fuel/air mixture preparation and sufficiently low to avoid fuel decomposition during mixture preparation. Measurements of the axial uniformity of the driven section inner wall temperature revealed that the driven section temperature variation was at ±2 °C.

2-Methylheptane/air and *n*-octane/air mixtures were prepared by direct injection of the liquid fuels into a heated mixing vessel followed by complete fuel evaporation, monitored via pressure, and the addition of O_2 and N_2 from compressed gas cylinders, at a molar ratio of 1:3.76. Fuel, O_2, and N_2 mixture fractions were specified via partial pressures. Liquid 2-methylheptane was procured from Eastern Sources at 99+% purity, liquid *n*-octane from Sigma Aldrich at 99+% purity, and O_2 and N_2 from Noble Gas Solutions both at 99.995% purity. Fuel/air mixtures were mechanical mixed inside the heated mixing vessel with a magnetically powered vane assembly for 20 min to 4 h prior to shock tube autoignition experiments.

Reflected shock ignition delay time measurements were made for *2*-methylheptane/air and *n*-octane/air mixtures at equivalence ratios of 0.5, 1.0, and 1.5 at pressures near 20 atm and for temperatures from 631 to 1327 K. To provide sufficient test times for low-temperature experiments with long ignition delay times (greater than approximately 1.5 ms), tailored N_2/He driver gas mixtures were used. For all other experiments, helium was used as the driver gas. Post-shock conditions were determined using the normal shock relations, known initial conditions, and measurement of the incident shock velocity made with a series of five pressure transducers located over the last meter of the driven section. The estimated uncertainty in the initial reflected shock conditions is ±1.5% in temperature and ±2.0% in pressure (90% confidence interval), with the primary contribution due to the uncertainty in measured incident shock velocity. Due to non-ideal gas dynamic interactions, pressure and temperature rise with time in all reflected shock experiments. In the experiments reported here the measured pressure gradient was dP/dt = 1-3%/ms. Assuming an isentropic relation between pressure and temperature this results in a temperature gradient of dT/dt = 0.3-0.8%/ms.

Ignition delay times were measured using both pressure and electronically-excited OH (OH*) chemiluminescence. Pressure was measured at a location 2 cm from the driven section end wall using a Kistler piezoelectric pressure transducer flush mounted in the driven section side wall. OH* chemiluminescence was measured through a fused silica optic located in the driven section end wall using a high-speed silicon photo detector and a UG5 Schott glass filter. The ignition delay time was defined as the time interval between shock arrival and reflection at the end wall (time-zero) and the onset of ignition at the end wall. Time-zero was determined using measurement of the time of shock passage at a pressure transducer located 2 cm from the end wall and the measured incident shock velocity and the onset of ignition at the end wall was defined by extrapolating the maximum slope in OH* emission to the baseline.

See Figure 6 for an example ignition delay time measurement for the experiment with the longest reported ignition delay time. The example in Figure 6 illustrates a well behaved (relatively flat) pressure profile prior to energy release and a two-stage autoignition, characteristic of low-temperature alkane kinetics and observed previously in shock tube experiments for n-heptane [63] and n-decane [64]. The estimated uncertainty in ignition delay times is ±25% (90% confidence interval), which accounts for contributions from uncertainties in reflected shock temperature and pressure, fuel/air mixture composition, and determining ignition delay times from measured signals.

3.3.2 Shock Tube Autoignition Results

Ignition delay time measurements are reported in the supplementary material and shown in Figure 7 and Figure 8 with comparisons to kinetic modeling. The results for both *2*-methylheptane and *n*-octane exhibit negative-temperature-coefficient (NTC) behavior characteristic of alkanes and decreasing ignition time with increasing equivalence ratio. Comparison of the data for the two C_8 isomers illustrates the influence of the single methyl substitution in *2*-methylheptane, which reduces reactivity, particularly in the NTC regime, consistent with the general understanding of the influence of branching on aliphatic oxidation. At high temperatures (T > 1000 K) and low temperatures (T < 750 K) the differences between *2*-methylheptane and *n*-octane ignition delay are relatively small (0-30%). On the other hand, in the NTC regime (750 K < T < 900 K) the differences are larger, with *2*-methylheptane having up to a factor of two longer ignition delay time compared to *n*-octane.

The proposed chemical kinetic model was validated against the shock tube ignition data using the homogenous batch reactor code in CHEMKIN PRO [56]. Simulations of the shock tube test environment included a 3%/ms pressure rise rate, which was imposed by providing a calculated volume history, as described by Chaos and Dryer [65]. Simulations with the imposed positive 3%/ms pressure rate are compared to simulations performed using the adiabatic constant volume constraint (no pressure rise) in Figure 8. The inclusion of the pressure rise has no influence on the simulations for temperatures greater than 1000 K. For temperatures from 700 to 1000 K the pressure rise results in a slight decrease (~25%) in simulated ignition delay. Only at the lowest temperatures studied (~650 K) does the pressure rise have a significant influence on simulated ignition delay (factor of two reduction).

Comparisons between experiment and kinetic model predictions illustrate that the model captures many of the experimental trends, including the difference in ignition delay for *2*-methylheptane and *n*-octane and the equivalence ratio dependence, but that modeling predictions for ignition delay are generally longer than experimental results for both compounds. At $\phi = 0.5$ the deviations between model and experiment range from within the experimental uncertainty in ignition delay (±25%) to a factor of two. At $\phi = 1.0$ and 1.5 the deviations in model and experiment are slightly larger and range from within

the experimental uncertainty to a factor of three. This level of deviation between shock tube ignition delay and kinetic modeling is typical of *a priori* modeling comparison with no tuning of reaction rate coefficients and is simply due to the large number of chemical reactions required to model the oxidation of hydrocarbon compounds found in liquid transportation fuels and uncertainties in both the selection of reaction pathways and prescription/estimation of reaction rate coefficients. The deviations in model and experiment appear to be primarily due to differences in the predicted and observed transition from high-temperature Arrhenius behavior with positive activation energy to NTC behavior and the transition from NTC to low-temperature behavior, where positive overall activation energy is again established. The turnover from high-temperature to NTC behavior is experimentally observed to occur around 900 K but predicted by the model to occur at 950 K. The transition from NTC to low-temperature behavior is observed to occur around 770 K but predicted to occur around 800 K. These differences in the predicted and observed temperature dependencies are relatively small (4-6% deviations in the two transition temperatures described above). Improvement to modeling predictions will require examination of the reactions responsible for the transitions in oxidation regimes, namely the overall peroxy reaction sequence, $R + O_2 \leftrightarrow RO_2 \leftrightarrow QOOH (+ O_2) \leftrightarrow OOQOOH \leftrightarrow 2OH$ + products, including the inhibitive direct (i.e., concerted) HO_2 elimination and QOOH decomposition routes.

3.3 Kinetic modeling simulations of shock tube ignition delay time for *n*-alkanes and *2*-methylkanes greater than C_8

In a previous study on *n*-alkanes [2], we presented kinetic modeling simulations of shock tube ignition delay time for *n*-alkanes from *n*-heptane (i.e., C_7) through *n*-hexadecane (i.e., C_{16}) at 13.5 bar initial pressure and stoichiometric conditions. The simulations at these conditions indicated that each fuel compound has virtually identical ignition delay times with only a slight trend in the NTC region of faster ignition delay times as the carbon chain length increases (i.e., increasing reactivity with increasing carbon number). The aforementioned results are surprising because one would expect ignition delay times to be observably different for longer chain alkanes. Biet et al. [66] also simulated ignition delay times of *n*-alkanes at 12 bar initial pressure and stoichiometric conditions; and showed that increasing the chain length slightly decreases ignition delay times at all temperatures.

In order to better understand the effects of carbon chain length on auto ignition properties of *n*-alkanes and *2*-methylalkanes, we conducted kinetic modeling simulations of shock tube ignition delay for even carbon number fuel compounds from C_8 to C_{16}. Since these compounds are important diesel fuel constituents, we conducted simulations at conditions that are relevant for diesel combustion applications. A phenomenological study of diesel combustion by Dec [67] indicates that in-cylinder pressures are in the region of 50 atm, and a rich equivalence ratio of 2 to 4 exists in the vapor-phase fuel region ahead of the

penetrating liquid jet where auto ignition occurs. This suggests that shock tube simulations at 12-13 bar initial pressure and stoichiometric conditions do not well represent the conditions under which diesel fuel ignition occurs in engines. Therefore, we conducted simulations were at initial pressures of 20 atm and rich equivalence ratios (i.e., $\phi = 3$) because these conditions are more relevant to practical applications.

Figure 9 presents the simulated ignition delay times for even carbon number *n*-alkanes and *2*-methylkanes from C_8 to C_{16}. The previous experimental and modeling section showed that *n*-octane exhibits faster ignition delay times than *2*-methylheptane; a similar decrease in reactivity is observed for larger *2*-methylalkanes when compared to *n*-alkanes of the same chain length. This trend agrees well with the lower DCN values measured for *2*-methylalkanes compared to *n*-alkanes of the same chain length (e.g., refer to Table 1). The simulations also indicate an observable decrease in ignition delay time as the size of the carbon chain increases from C_8 to C_{10} to C_{12}. However, *n*-tetradecane (C_{14}) and *n*-hexadecane (C_{14}) exhibit similar reactivity at all temperatures, which suggests that the adding carbon atoms does not increase reactivity after the carbon chain reaches a critical length. A similar diminishing returns is observed for the *2*-methylkalkanes, wherein *2*-methylundecane (C_{12}). 2-methyltridecane (C_{14}), and 2-methylpentadecane (C_{16}) all exhibit similar reactivity. Although not shown, simulations for *2*-methylheptadecane (C_{18}) and *2*-methylheptadecane (C_{20}) also showed similar reactivity as the C_{12} - C_{16} compounds. These simulated observations are generally consistent with experimentally measured cetane numbers that indicate a large increase in cetane number from *n*-octane (C_8 CN = 65) to *n*-tetradecane (C_{14} CN = 96), followed by much smaller increases as the carbon chain length increases above C_{14} (e.g., C_{16} CN = 100, C_{18} CN = 110, C_{20} CN = 110) [68]. Although kinetic effects play a role in diesel engine ignition delay (i.e., cetane number rating), the physical effects (e.g., density, vapor pressure) on spray combustion are also important factors to consider. Therefore, the conclusions drawn here from kinetic modeling simulations should be considered in conjunction with physical contributions of chain length on a fuel's cetane number.

3.5 Laminar Flame Speed Experiments and Simulations of *n*-octane and 2-methylheptane

3.5.1 Laminar Flame Speed Experimental Setup

Laminar flame speed, S_u^0, experiments were carried out for *2*-methylheptane at the University of Southern California in the counterflow configuration at atmospheric pressure and an unburned reactant temperature of 353 K. Details of the experimental configuration and the fuel vaporization system have been described extensively in previous studies by the authors [69-73]. In order to determine S_u^0's the symmetric twin-flame configuration was used. The flow was seeded with 0.3-μm diameter silicon oil droplets, and the axial flow velocities were measured along the stagnation streamline using digital particle image velocimetry.

In order to determine S_u^0, the minimum point of the axial velocity profile just upstream of the flame is measured and defined as the reference velocity, $S_{u,ref}$, and the absolute value of the maximum velocity gradient in the hydrodynamic zone is defined as the imposed strain rate, K, [72]. S_u^0 is subsequently determined through non-linear extrapolation of $S_{u,ref}$ to $K = 0$, using a computationally-assisted approach [71,73]. The standard deviation (2σ) in the determination of S_u^0 was quantified and is indicated with the appropriate bars in all figures. In general, the uncertainties in $S_{u,ref}$ for fuel-rich flames are larger than those of lean and near-stoichiometric flames. The uncertainty in ϕ is no larger than 0.5%.

3.5.2 Laminar Flame Speed Results of 2-methylheptane and n-octane

Figure 10 depicts both experimental data and numerical predictions for the S_u^0's of *2*-methylheptane/air and *n*-octane/air flames; the experimental data for *n*-octane/air flames were taken from [53]. S_u^0's of *2*-methylheptane/air flames are consistently 3.5-5 cm/s lower than those of *n*-octane/air flames. This is expected, as it has previously established experimentally (e.g., [53,74-76]) that branching in the fuel molecular structure reduces reactivity and as a result S_u^0.

Chemical kinetic modeling simulations of laminar flame speed were conducted using the PREMIX code in CHEMKIN PRO [56]. A high-temperature C_8 version of the detailed mechanism was used for these simulations, wherein species greater than C_8 and reaction classes 11-30 were removed. The simulations accounted for thermal diffusion, assumed mixture-averaged transport, and the solutions were highly resolved with approximately 200 grid points. The current model reproduces successfully the relative reactivities of these two fuels. The peak S_u^0 for both *n*-octane/air and 2-methylheptane/air flames occurs at $\phi \approx 1.05$. The predictions of the current model are in good agreement with the experimental data for *2*-methylheptane flames for $0.70 \leq \phi \leq 1.10$. At higher ϕ's, the model is over predicting the experimental results by approximately 4 cm/s. For *n*-octane/air flames, the agreement between the model and the experimental data taken from [53] are good for rich to stoichiometric conditions, and the model consistently under predicts the experimental results for fuel lean conditions. Figure 11 presents *n*-octane/air premixed laminar flame velocities at range of pressures [54] as an additional validation target for the proposed mechanism. The model exhibits excellent agreement with the experimental data at 1 atm and 2 atm. At 5 atm, the model under predicts the laminar flame velocity at equivalence rations greater than 0.9.

In order to elucidate the reasons for lower flame speeds in *2*-methylheptane, a reaction flux analysis was conducted for *2*-methylheptane and *n*-octane at stoichiometric conditions and a temperature of approximately 1000 K. We do not present a figure of the flux analysis because the results are similar to those presented in a previous flame study by Sarathy et al. [28]. The results show that H-atom abstraction from the tertiary C-H site in *2*-methylheptane followed by β-scission leads to the formation of

iso-butene and subsequently the resonantly stabilized *iso*-butenyl radical. An analogous reaction sequence in *n*-octane leads to 1-butene and subsequently the *1*-butenyl radical. The increased stability of the *iso*-butenyl radical compared to the *1*-butenyl is the reason for lower flame speeds in *2*-methylheptane. This trend towards lower reactivity of *2*-methylalkanes in premixed flame systems is expected to remain for higher molecular weight compounds, as a previous study [53] has shown that laminar flame speeds are similar among *n*-alkanes from C_7 to C_{12}.

3.6 2-Methylheptane Model Reduction and Counterflow Flame Ignition and Extinction

The previous validation studies all dealt with premixed reacting flows. However it is important to also validate the proposed model against non-premixed aerodynamically strained reacting flows because these conditions are often found in practical combustion applications. Flame extinction in strained flows is relevant to gas turbine engines, while flame ignition in strained flows is relevant to ignition in high swirl internal combustion engines. This section presents experimental data and simulated results for flame extinction and ignition in the for counterflow configuration. Performing simulations of counterflow experiments with large chemical kinetic models is time consuming, highly demanding in computer memory requirements, and difficult to search for initial converged solutions. To minimize these difficulties, we reduced the size of the detailed chemical kinetic model.

3.6.1 Mechanism reduction

The reduced chemical kinetic mechanism for *2*-methylheptane was created by first manually eliminating reaction pathways for all species greater than C_8 from a high temperature version of the complete mechanism. The resulting "detailed" high temperature mechanism for *2*-methylheptane consists of 714 species and 3397 elementary reaction steps. Then the mechanism was further reduced automatically using the method of directed relation graph (DRG) [77,78] to eliminate unimportant species and reactions for flame simulations. The DRG method quantifies species couplings as the pair-wise relative error induced to one species by the elimination of another. It then systematically identifies the species that are strongly coupled to the major species, such as the fuel, oxidizer, and important radicals, through a linear-time revised depth-first search (RDFS) method [79]. In a recent study [78], the DRG method was further improved by redefining the pair-wise relative error to species *A* induced by the elimination of species *B* as:

$$r_{AB} \equiv \frac{\max_i \left| \nu_{A,i} \omega_i \delta_{Bi} \right|}{\max_i \left| \nu_{A,i} \omega_i \right|} \quad , \quad \delta_{Bi} = \begin{cases} 1, & \text{if the ith reaction involves B} \\ 0, & \text{otherwise} \end{cases} , \tag{1}$$

where ω_i is the net reaction rate of the *i*th reaction and $\nu_{A,i}$ is the stoichiometric coefficient of species *A* in the *i*th reaction. It was shown in Ref. [78] that the definition of r_{AB} in eq. (1) is more advantageous than that in the original DRG method [77] when the detailed mechanism consists of a large number of isomers, e.g. that in the present mechanism for 2-methylheptane and other engine fuels with long chains.

The reduction was performed based on reaction states sampled in a parameter range that is relevant to the ignition and extinction of the counterflow flames in the present work. The reaction states for ignition study were sampled from auto-ignition calculated with SENKIN [80], and reaction states for extinction were sampled from perfectly stirred reactors (PSR) [81]. Both applications were simulated under atmospheric pressure for 2-methylheptane – air mixtures with equivalence ratios between 0.5 and 2.0. The initial temperature for ignition was set to be 1000 K - 1800 K. The inlet temperature for PSR was fixed at 300 K, which gave reactor temperatures of 1000 K - 2300K for 1 atm and the stoichiometry considered. These temperature ranges were chosen to cover the temperature ranges expected in the extinction and ignition experiments in the counterflow apparatus.

It is noted that although the non-premixed counterflow flames may involve mixtures with arbitrary equivalence ratios, previous studies indicate that mechanisms reduced in the above range of equivalence ratio are typically applicable to non-premixed flames in predicting such limit phenomena as ignition and extinction [82]. This is primarily because the reaction zone of a non-premixed flame tends to be located near the stoichiometric surface, and mixtures far away from the reaction zone are typically dominated by the transport processes rather than chemistry. It is further noted that the ignition of counterflow flames was found to be insensitive to low-temperature chemistry [77,83,84]. Therefore the present reduced mechanism developed for high temperatures (above 1000 K) is adequate for the counterflow ignition study in the present work, while it should not be applied where low-T chemistry is important, e.g., oxidation in JSR or ignition in RCM and homogeneous charge compression ignition (HCCI) engines.

The number of species in the skeletal mechanism as a function of the threshold value, ε, to truncate the r_{AB} values in eq. (1) based on the sampled reaction states is shown in Figure 12. By specifying a critical value of ε=0.3, which is roughly equivalent to the worst-case relative error of about 23% based on the definition of r_{AB} in the original DRG method [77], a skeletal mechanism with 151 species and 989 reactions was obtained. While further reduction can be achieved either by further increasing the error threshold or by employing other reduction methods such as DRG aided sensitivity analysis (DRGASA) [84,85], the 151-species skeletal mechanism was selected to simulate the counterflow flames in the present work considering that such a mechanism size is affordable for the present simulations and it is important to avoid unnecessary loss in chemical fidelity for the analysis of detailed reaction pathways.

For mechanism validation, Figure 13 shows the temperature profiles for PSR and auto-ignition within the parameter range of the reduction, calculated with the 151-species and the detailed mechanisms, respectively. It is seen that the skeletal mechanism agrees closely with the detailed mechanism, with a worst-case error of approximately 20% observed in the extinction time of the PSR. It is further seen that the skeletal mechanism not only accurately predicts the global parameters of ignition delay and extinction time, but also reproduces the detailed structure of the temperature profiles. This implies that the important species and reaction pathways were correctly retained in the reduction for various stages of the oxidation. In the following, the mechanism will be employed to predict ignition and extinction of 1-D counterflow diffusion flames.

3.6.2 Counterflow Flame Experimental Setup

Extinction and auto-ignition of non-premixed flames of *2*-methylheptane were measured employing the counterflow configuration. Figure 14 shows a schematic illustration of the counterflow configuration. Steady, axisymmetric, laminar flow of two counterflowing streams toward a stagnation plane is considered. In this configuration, a fuel stream made up of prevaporized *2*-methylheptane and nitrogen is introduced through the bottom duct, and an oxidizer stream of air is injected through the upper duct. A mixing-layer develops around the stagnation plane. The exit of the fuel duct is called the fuel boundary and the exit of the oxidizer duct the oxidizer boundary. Fine wire screens are located at the exits of the ducts. As a consequence, the tangential component of the flow velocities vanishes at the boundaries. This allows the use of ‘‘plug flow boundary conditions” in numerical simulations. The mass fraction of fuel, temperature, and the component of the flow velocity normal to the stagnation plane at the fuel boundary are represented by $Y_{F,1}$, T_1, and V_1, respectively. The mass fraction of oxygen, temperature, and the component of the flow velocity normal to the stagnation plane at the oxidizer boundary are represented by $Y_{O_2,2}$, T_2, and V_2, respectively. The exit diameter of the fuel duct and the oxidizer duct is 23 mm. L represents the distance between the fuel boundary and the oxidizer boundary. The value of the strain rate, defined as the normal gradient of the normal component of the flow velocity, changes from the fuel boundary to the oxidizer boundary. The characteristic strain rate on the oxidizer side of the stagnation plane a_2 is given by Equation 2 [88]

$$a_2 = \frac{2|V_2|}{L}\left(1 + \frac{|V_1|\sqrt{\rho_1}}{|V_2|\sqrt{\rho_2}}\right) \quad (2)$$

Extinction experiments were conducted with a duct separation of L = 10mm, and T_2 = 298 K. The temperature of the fuel stream, T_1, for all fuels is 400K. At some selected value of $Y_{F,1}$, the flame was

stabilized. The strain rate was increased by increasing V_1 and V_2 simultaneously, keeping momenta of the counterflowing streams balanced based on $\rho_1 V_1^2 = \rho_2 V_2^2$ until extinction was observed.

Auto-ignition experiments were carried out with a duct separation of L = 12mm, a fuel stream temperature of 400K (±5K) and a fuel mass fraction, $Y_{F,1}$=0.4. For selected values of strain rate a_2 the oxidizer stream temperature was increased until auto-ignition took place. The velocities of the counterflowing streams were constantly adjusted based on the change in temperature to satisfy the momentum balance equation.

The accuracies of the strain rate and fuel mass fraction were 5% and 3% of the recorded values, respectively. The experimental repeatability of the reported strain rate at extinction was 3% of recorded value. The accuracy of the measurement of the oxidizer temperature was determined to be ±20K. The experimental repeatability on recorded temperature of air at auto-ignition was ±5K.

3.6.3 2-Methylheptane Counterflow Flame Ignition and Extinction Results

The skeletal mechanism was used to compute critical conditions of extinction and ignition, and the results were compared to the experiments. The extinction computations were carried out using extinction solver in CHEMKIN PRO [56], which uses the arc length continuation method to generate the S-shaped response curve [37, 38]. Plug flow boundary conditions were employed in the calculations. For a give composition and temperature of the reactant streams at the boundaries, the flow velocities V_1 and V_2 were increased until extinction takes place. The strain rate at extinction is calculated using Equation (1). Ignition calculations were performed using the OPPDIF solver in CHEMKIN PRO using the following procedure. We made an initial guess for the temperature profile and computed a fully resolved, cold solution temperature profile. Then we used the cold solution temperature profile as an initial guess and iteratively increased the temperature of air at the boundary, T_2, in the simulations until ignition took place. The composition of the reactant streams, their flow velocities and the value of the fuel stream temperature, T_1, were all maintained constant during this procedure. The strain rate at ignition was calculated using Equation (1).

Figure 15 shows the mass fraction of fuel, $Y_{F,1}$, as a function of the strain rate at extinction, a_2,e. The symbols in this figure represent experimental data and the line represents the calculations. They separate a flammable region for $a_2 < a_{2,e}$ from a nonflammable region for $a_2 > a_{2,e}$. At a given value of strain rate the calculated fuel mass fraction at extinction is slightly higher than the measured value, but the overall agreement is considered excellent. Figure 16 shows the temperature of air at ignition, $T_{2,I}$, as a function of the strain rate, a_2, for values of $Y_{F,1}$ = 0.4. The symbols represent experimental data with both uncorrected and corrected temperatures presented. The line represents results of numerical calculations using the skeletal mechanism. It separates a region for $T_2 > T_{2,I}$ where ignition can take place from a

region where ignition is not possible. For a given a_2, the calculated value of $T_{2,I}$ is lower than the measured temperature corrected for radiation losses. Considering the error on the temperature measurements is ±20 K, the model predictions are considered to be excellent.

4. Conclusions and Outlook

This study presented a comprehensive experimental and modeling study for the oxidation of *2*-methylkanes and *n*-alkanes larger than C_8. New experimental data was presented for *2*-methylheptane in a jet stirred reactor, shock tube, premixed laminar fame, and counterflow diffusion flame. The detailed mechanism exhibited good agreement with the various sets of experimental data. A skeletal mechanism derived from the detailed mechanism well reproduced counterflow flame extinction and ignition experimental data.

Jet stirred reactor experiments and model predictions indicate that branched alkenes (i.e., *2*-methyalkenes) are important intermediates in the oxidation of *2*-methylheptane. The experimentally observed cool flame reactivity, NTC behavior, and transition to high temperature oxidation are all well predicted by the proposed model. Transitions between chain branching peroxy chemistry, concerted elimination reactions, cyclic ether formation, and β-scission reactions are responsible controlling the overall reactivity of the *2*-methylheptane oxidation system.

Both the experiments and model predictions indicate that *2*-methylalkanes have longer shock tube ignition delay times than *n*-alkanes of the same chain length. Simulations conducted under diesel relevant conditions indicate that the reactivity of *2*-methylkalkanes and *n*-alkanes increase with increasing carbon number; however, a plateau in reactivity is achieved at approximately C_{14}. Experimental ignition data at high pressures and rich conditions are needed to verify these model predicted trends.

Premixed laminar flame speeds are slower for *2*-methylheptane when compared to *n*-octane because of the increased production of the resonantly stabilized *iso*-butenyl radical. This trend towards lower reactivity of *2*-methylalkanes in premixed flame systems is expected to remain for higher molecular weight compounds. The present study has also exhibited the potential of using computational techniques to reduce the detailed mechanism and well predict one-dimensional counterflow diffusion flame ignition and extinction data.

The proposed *2*-methylkalkane/*n*-alkane chemical kinetic mechanism has the potential of significantly improving our understanding diesel and jet fuel combustion. The structures present within the mechanism can be used to develop surrogate fuel formulations for a wide variety of fuels, such as conventional petroleum derived fuels, synthetic Fischer-Tropsch fuels, and renewable fuels derived from thermochemical treatment of bio-derived fats and oils (e.g., HRJ fuels). For example, previous studies that developed surrogate kinetic models for jet-A [89] and F-T jet fuels (e.g., S-8) [90,91] only had the

option of using a highly branched molecule, *iso*-octane, as the surrogate for the lightly branched alkanes found in real fuels because detailed kinetic models for latter were unavailable at the time. Therefore, the present study provides immediate potential of improving the chemical fidelity of surrogate fuel models.

In addition to improving surrogate fuel models, this study provides fundamental information on the effects of methyl branching. We aim to advance this understanding by determining the effects methyl branch location and number by extending the proposed mechanism to include other lightly branched alkanes (e.g., *3*-methylalkanes and dimethylalkanes) that are also present in real fuels. The inclusion of these additional species will undoubtedly increase the size and complexity of our models. Therefore, we encourage and are actively pursuing the use of mechanism reduction techniques to decrease the size of the detailed mechanism, and thus enable their use in three-dimensional computational fluid dynamics (3D-CFD) engine-like simulations [92,93].

5. Acknowledgments

The authors thank National Renewable Energy Laboratory researchers Matthew Ratcliffe and Jon Luecke, as well as Gregory Bogin, Jr. from the Colorado School of Mines for providing unpublished derived cetane numbers for *n*-alkanes and *2*-methylkanes. The work at LLNL work was supported by the US Department of Energy, Office of Vehicle Technologies and the Office of Basic Energy Sciences, and the authors thank program managers Gurpreet Singh, Kevin Stork, and Wade Sisk. This work was performed under the auspices of the US Department of Energy by Lawrence Livermore National Laboratory under Contract DE-AC52-07NA27344. The research at the University of California at San Diego was supported by the U. S. Army Research Office, Grant # W911NF-09-1-0108, Program Manager Dr. Ralph A. Anthenien Jr.. The work at University of Connecticut was supported by the National Science Foundation under Grant 0904771. The coauthor S.M.S. acknowledges fellowship support from the Natural Science and Engineering Research Council of Canada (NSERC).

6. Supplemental Material

This publication includes the following supplemental material:

1. A complete description of the detailed chemical kinetic mechanism reaction pathways and reaction rate rules.
2. Raw experimental data for shock tube ignition delay measurements of *n*-octane and *2*-methylheptane.
3. A complete detailed chemical kinetic mechanism covering high and low temperature reactivity of *n*-alkanes up to C_{16} and *2*-methylalkanes up to C_{20} in CHEMKIN format. (.INP format)

4. A detailed chemical kinetic mechanism covering high and low temperature reactivity of *n*-alkanes and *2*-methylalkanes up to C_8 in CHEMKIN format (.INP format)
5. A smaller detailed chemical kinetic mechanism covering high temperature reactivity of *n*-alkanes and *2*-methylalkanes up to C_8 in CHEMKIN format (.INP format)
6. A 151-species skeletal mechanism for *2*-methylheptane generated using the DRG methodology (.INP format)
7. The proposed thermodynamic datafile in CHEMKIN format. (.DAT format)
8. The proposed transport datafile in CHEMKIN format. (.DAT format)

7. References

1. H.J. Curran, P. Gaffuri, W.J. Pitz, C.K. Westbrook, Combust. Flame 114 (1998) 149-177.
2. C.K. Westbrook, W.J. Pitz, O. Herbinet, H.J. Curran, E.J. Silke, Combust. Flame 156 (2009) 181-199.
3. H.J. Curran, P. Gaffuri, W.J. Pitz, C.K. Westbrook, Combust. Flame 129 (2002) 253-280.
4. M.A. Oehlschlaeger, J. Steinberg, C.K. Westbrook, W.J. Pitz, Combust. Flame 156 (2009) 2165-2172.
5. C.K. Westbrook, W.J. Pitz, J.E. Boercker, H.J. Curran, J.F. Griffiths, C. Mohamed, M. Ribacour, Proc. Combust. Inst. 29 (2002) 1311-1318.
6. C.K. Westbrook, W.J. Pitz, H.J. Curran, J. Boercker, E. Kunrath, Int. J. Chem. Kinet. 33 (12) (2001) 868-877.
7. M. Mehl, G. Vanhove, W.J. Pitz, E. Ranzi. Combust. Flame 155 (4) (2008) 756-772.
8. M. Mehl, W.J. Pitz, C.K. Westbrook, K. Yasunaga, C. Conroy, H.J. Proc. Combust. Inst. 33
9. (2011) 201-208.
10. M. Mehl, W.J. Pitz , C.K. Westbrook, H.J. Curran, Proc. Combust. Inst. 33 (2011) 193-200.
11. E.J. Silke, W.J. Pitz, C.K. Westbrook, J. Phys. Chem. A 111 (2007) 3761-3775.
12. W.J. Pitz, C.V. Naik, T.N. Mhaolduin, C.K. Westbrook, H.J. Curran, J.P. Orme, J.M. Simmie, Proc. Combust. Inst. 31 (2007) 267-275.
13. M. Mehl, W. J. Pitz, M. Sjöberg, J. E. Dec, SAE 2009 International Powertrains, Fuels and Lubricants Meeting, SAE Paper No. 2009-01-1806, Florence, Italy.
14. C.K. Westbrook, W.J. Pitz, M. Mehl, H.J. Curran, Proc. Combust. Inst. 33 (2011) 185-192.
15. W.J. Pitz, C.J. Mueller, Prog. Energy Comb. Sci. (2010), doi:10.1016/j.pecs.2010.06.004.
16. M. Alnajjar, B. Cannella, H. Dettman, C. Fairbridge, J. Franz, T. Gallant, R. Gieleciak, D. Hager, C. Lay, S. Lewis, M. Ratcliff, S. Sluder, J. Storey, H. Yin, B. Zigler, CRC Report No. FACE-1 (2010), Coordinating Research Council, Inc., Alpharetta, GA.

17. B.L. Smith, T.J. Bruno, J. Propulsion 24 (3) (2008) 619-623.
18. B.L. Smith, T.J. Bruno, Ind. Eng. Chem. Res. 46 (1) (2007) 310-320.
19. G. Knothe, Prog. Ener. Combust. Sci. 36 (2010) 364–373.
20. R. Wilk, W.J. Pitz, C.K. Westbrook, S. Addagarla, D.L. Miller, N.P. Cernansky, R.M. Green, Proc. Combust. Inst. 23 (1990) 1047-1053.
21. T. Ogura, Y. Nagumo, A. Miyoshi, M. Koshi, Energy Fuels, 21 (2007) 130-135.
22. M.A. Oehlschlaeger, D.F. Davidson, J.T. Herbon, R.K. Hanson, Int. J. Chem. Kinet. 36 (2) (2004) 67-78.
23. D. Healy, N.S. Donato, C.J. Aul, E.L. Petersen, C.M. Zinner, G. Bourque, H.J. Curran, Combust Flame 157 (2010) 1540-1551.
24. A. Burcat, E. Olchanski, C. Sokolinski, Combust. Sci. and Tech. 147 (1999) 1-37.
25. J.F. Griffiths, J.P. MacNamara, C.G.W. Sheppard, D.A. Turton, B.J. Whitaker, Fuel 81 (2002) 2219–2225.
26. E.J. Silke, H.J. Curran, J.M. Simmie, Proc. Combust. Inst. 30 (2005) 2639–2647.
27. M.S.P. Kahandawala, M.J. DeWitt, E. Corporan, S.S. Sidhu, Energy Fuels 22 (2008) 3673-3679.
28. S.M. Sarathy, C. Yeung, C.K. Westbrook, W.J. Pitz, M. Mehl, M.J. Thomson. Combust. Flame. (2010) dx.doi.org/10.1016/j.combustflame.2010.11.00
29. ASTM D 6890, ASTM International, West Conshohocken, PA, 2007.
30. L.N. Allard, N.J. Hole, G.D. Webster, T.W.I. Ryan, D. Ott, A. Beregszazy, C.W. Fairbridge, J. Cooley, K. Mitchell, E.K. Richardson, N.G. Elliot, D.J. Rickeard, SAE Tech. Pap. (1997) 971636.
31. L.N. Allard, G.D. Webster, T.W.I. Ryan, A. Matheaus, G. Baker, A. Beregszazy, H. Read, K. Mortimer, G.J. Jones, SAE Tech. Pap. (2001) 2001013527.
32. M.V. Johnson, S.S. Goldsborough, Z. Serinyel, et al., Energy Fuels 23 (2009) 5886–5898.
33. J. Moc, G. Black, J.M. Simmie, H.J. Curran, AIP Conf. Proc. 1148 (2009) 161–164.
34. W.S. McGivern, I.A. Awan, W. Tsang, J.A. Manion, J. Phys. Chem. A 112 (2008) 6908-6917.
35. W. Tsang, J.A. Walker, J.A. Manion, Proc. Combust. Inst. 32 (2007) 141–148.
36. W. Tsang, W.S. McGivern, J.A. Manion, Proc. Combust. Inst. 32 (2009) 131–138.
37. I.A. Awan, W.S. McGivern, W. Tsang, J.A. Manion, J. Phys. Chem. A 114 (2010) 7832-7846.
38. L. Zhu, J.W. Bozzelli, L.M. Kardos, J. Phys. Chem. A. 111 (2007) 6361-6377.
39. G. E. Quelch, M. M. Gallo, M. Z. Shen, Y. M. Xie, H. F. Schaefer, D. Moncrieff, J. Am. Chem, Soc. 116 (11) (1994) 4953-4962.
40. E. J. Silke, W. J. Pitz, C. K. Westbrook, M. Ribaucour, J. Phys. Chem. A 111 (19) (2007) 3761-3775.

41. E.R. Ritter, J.W. Bozelli, Int. J. Chem. Kin. 23 (1991) 767-778.
42. S.W. Benson, Thermochemical Kinetics (2nd ed.), Wiley, New York (1976).
43. T.H. Lay, J.W. Bozzelli, A.M. Dean, E.R. Ritter, J. Phys. Chem. 99 (1995) 14514-14527.
44. Bozzelli, J. W. Personal communication, new THERM version, 2003.
45. L.S. Tee, S. Gotoh, W.E. Stewart, Ind. Eng. Chem. Fundam. 5 (3) (1966) 356-363.
46. A.T. Holley, Y. Dong, M.G. Andac, F.N. Egolfopoulos, Combust. Flame 144 (2006) 448-460.
47. I. Owczarek, K. Blazej, J. Phys. Chem. Ref. Data, 32 (4) (2003) 1411-1427.
48. I. Owczarek, K. Blazej, J. Phys. Chem. Ref. Data, 35 (4) (2006) 1461-1474.
49. S.M. Sarathy, M.J. Thomson, W.J. Pitz, T. Lu, Proc. Combust. Inst. 33 (2011) 399-405.
50. R. Bosque, J. Sales, J. Chem. Inf. Comp. Sci. 42 (2002) 1154-1163.
51. D. R. Lide (Ed.), CRC Handbook of Chemistry and Physics, 87th Edition, Taylor and Francis, Boca Raton, FL, 2007.
52. A.L. McClellan, Tables of Experimental Dipole Moments, Freeman, San Francisco, 1963.
53. C. Ji, E. Dames, Y.L. Wang, H. Wang, F.N Egolfopoulos, Combust. Flame 157 (2010) 277–287.
54. A. Kelley, W. Liu, Y. Xin, A. Smallbone, and C. Law, Proc. Combust. Inst., 33 (2010), 501-508.
55. E.J. Silke, Ph.D. thesis, National University of Ireland, Galway, 2005.
56. CHEMKIN-PRO Release 15101, Reaction Design, Inc, San Diego, CA, 2010.
57. S. Dooley, H.J. Curran, J.M. Simmie, Combust. Flame 153 (2008) 2–32.
58. P. Dagaut, M. Cathonnet, J.P. Rouan, R. Foulatier, A. Quilgars, J.C. Boettner, F. Gaillard, H. James, Journal of Physics E: Instrum. 19 (1986) 207-209.
59. G. Dayma, S. M. Sarathy, C. Togbé, C. Yeung, M. Thomson, P. Dagaut, Proc. Combust. Inst. 33 (1) (2011) 1037-1043.
60. P. Dagaut, M. Reuillon, M. Cathonnet, D. Presvots, Chromatographia 40 (1995) 147-154.
61. O. Herbinet, S. Bax, P.-A. Glaude, V. Carré, F. Battin-Leclerc, Fuel 90 (2) (2011) 528-535
62. H.-P.S. Shen, M.A. Oehlschlaeger, Combust. Flame 156 (2009) 1053–1062.
63. H.K. Ciezki, G. Adomeit, Combust. Flame 93 (1993) 421-433.
64. U. Pfahl, K. Fieweger, G. Adomeit, Proc. Combust. Inst. 26 (1996) 781-789.
65. M. Chaos, F.L. Dryer, Int. J. Chem. Kin. 42 (2010) 143-150.
66. J. Biet, M.H. Hakka, V. Warth, P.-A. Glaude, F. Battin-Leclerc, Energy Fuels 22 (2008) 258-2269.
67. J.E. Dec, (1997) SAE Paper 970873, 1-30.
68. M.J. Murphy, J.D. Taylor, R.L. McCormick, “Compendium of Experimental Cetane Number Data”, NREL/SR-540-36805, National Energy Renewable Laboratory (2004) Golden, Colorado, USA.

69. A. T. Holley, Y. Dong, M. G. Andac, F. N. Egolfopoulos, Combust. Flame 144 (2006) 448–460.
70. A.T. Holley, Y. Dong, M.G. Andac, F.N. Egolfopoulos, T. Edwards, Proc. Combust. Inst. 31 (2007) 1205–1213.
71. P.S. Veloo, Y.L. Yang, F.N. Egolfopoulos, C.K. Westbrook, Combust. Flame 157 (2010) 1989-2004.
72. C. K. Wu, C.K. Law, Proc. Comb. Inst. 20 (1984) 1941–1949.
73. Y.L. Wang, A.T. Holley, C. Ji, F.N. Egolfopoulos, T.T. Tsotsis, H.J. Curran, Proc. Combust. Inst. 32 (2009) 1035–1042.
74. S.G. Davis, C.K. Law, Combust. Sci. Technol. 140 (1998) 427–449.
75. P.S. Veloo, F.N. Egolfopoulos, Combust. Flame 158 (2011) 501–510.
76. P.S. Veloo, F.N. Egolfopoulos, Proc. Combust. Inst. 33 (2011) 987–993.
77. T.F. Lu, and C.K. Law, Proc. Combust. Inst., 30 (2005), 1333-1341.
78. Z. Luo, T. Lu, M. Maciaszek, S. Som, and D. Longman, Energy Fuels, 24 (2010), 6283–6293.
79. T.F. Lu, and C.K. Law, Combust. Flame, 144 (2006), 24-36.
80. A.E. Lutz, R.J. Kee, and J.A. Miller, Technical Report SAND87-8248, Sandia National Laboratories (1987).
81. P. Glarborg, R. Kee, J. Grcar, and J. Miller, SAND86-8209, Sandia National Laboratories (1986).
82. T.F. Lu, and C.K. Law, Prog. Energy Combust. Sci., 35 (2009), 192-215.
83. K. Seshadri, T.F. Lu, O. Herbinet, S.B. Humer, U. Niemann, W.J. Pitz, R. Seiser, and C.K. Law, Proc. Combust. Inst., 32 (2009), 1067-1074.
84. X.L. Zheng, T.F. Lu, and C.K. Law, Proc. Combust. Inst., 31 (2007), 367-375.
85. R. Sankaran, E.R. Hawkes, J.H. Chen, T.F. Lu, and C.K. Law, Proc. Combust. Inst., 31 (2007), 1291-1298.
86. V. Giovangigli and M. D. Smooke, Combust. Sci. Technol. 53 (1) (1987) 23-49.
87. M. Nishioka, C. K. Law and T. Takeno, Combust. Flame 104 (3) (1996) 328-342.
88. K. Seshadri, F. Williams, Int. J. Heat Mass Trans. 21 (1978) 251-253.
89. S. Dooley, S.H. Won, M. Chaos, J. Heyne, Y. Ju, F.L. Dryer, K. Kumar, C.-J. Sung, H. Wang, M.A. Oehlschlaeger, R.J. Santoro, T.A. Litzinger, Combustion and Flame 157 (2010) 2333–2339
90. C.V. Naik, K.V. Puduppakkam, A. Modak, E. Meeks, Y.L. Wang, Q. Feng, T.T. Tsotsis, Combustion and Flame 158 (2011) 434–445.
91. P. Gokulakrishnan, M.A. Klassen, R.J. Roby, ASME Turbo Expo (2008) #GT2008-51211, Berlin, Germany
92. Y. Ra, R. Reitz, Combustion and Flame 158 (2011) 69–90.
93. Y. Ra, R. Reitz, Combustion and Flame 155 (2008) 713–738

List of Tables

List of Figures

Figure 14 - Schematic illustration of the counterflow flow field

Figure 15 - The mass fraction of fuel, $Y_{F,1}$, as a function of the strain rate at extinction, $a_{2,e}$ in the counterflow flame. The symbols represent experimental data. The line is results of numerical calculation using the skeletal mechanism.

Figure 16 - The temperature of the oxidizer stream at ignition, T2,I, as a function of the strain rate, a2 for YF,1 = 0.4 in the counterflow flame. The symbols represent experimental data. The line is result of numerical calculations using the skeletal mechanism.

Table 1 – Derived Cetane number (DCN) values for *n*-alkanes and *2*-methylallkanes.

Compound	Ignition Delay (ms), NREL *	DCN, NREL*
n-heptane (nC_7H_{18})	3.784	53.8
2-methylhexane (C_7H_{18}-2)	4.775	43.5
n-octane (nC_8H_{18})	3.513	57.6
2-methylheptane (C_8H_{18}-2)	3.881	52.6

* Unpublished results from the National Energy Renewable Laboratory 2007-2010; all DCNs from D6890-06 equation; DCN = 4.460 + 186.6/ID

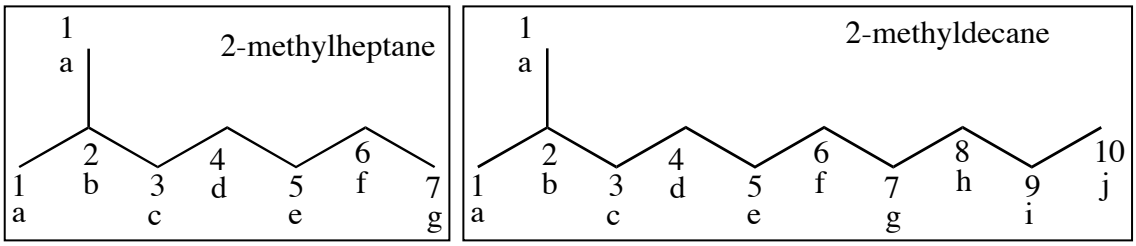

Figure 1 - Structure of *2*-methylheptane (C_8H_{18}-2) and *2*-methyldecane ($C_{11}H_{24}$-2)

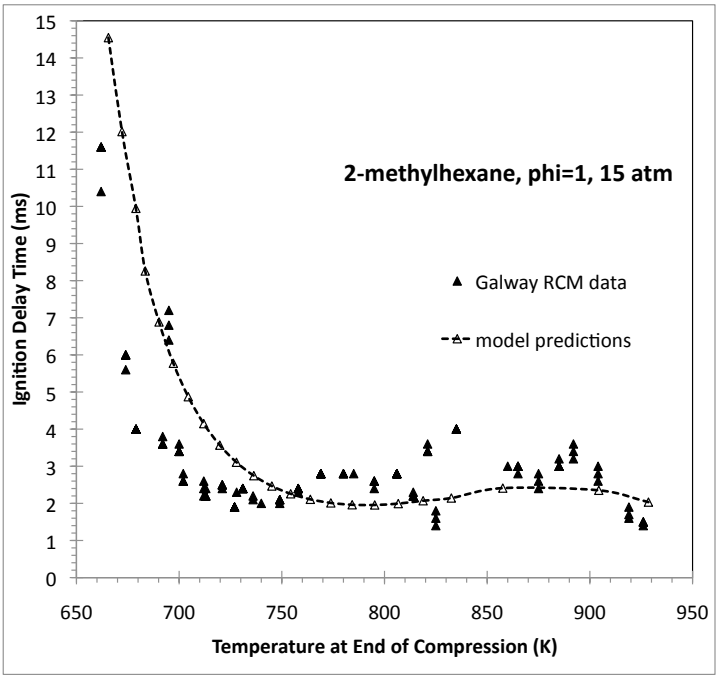

Figure 2 – Experimental (Silke et al., Proc. Combust. Inst. 2005) and simulated ignition delay times for 2-methylhexane. P = 15 atm, phi = 1.0.

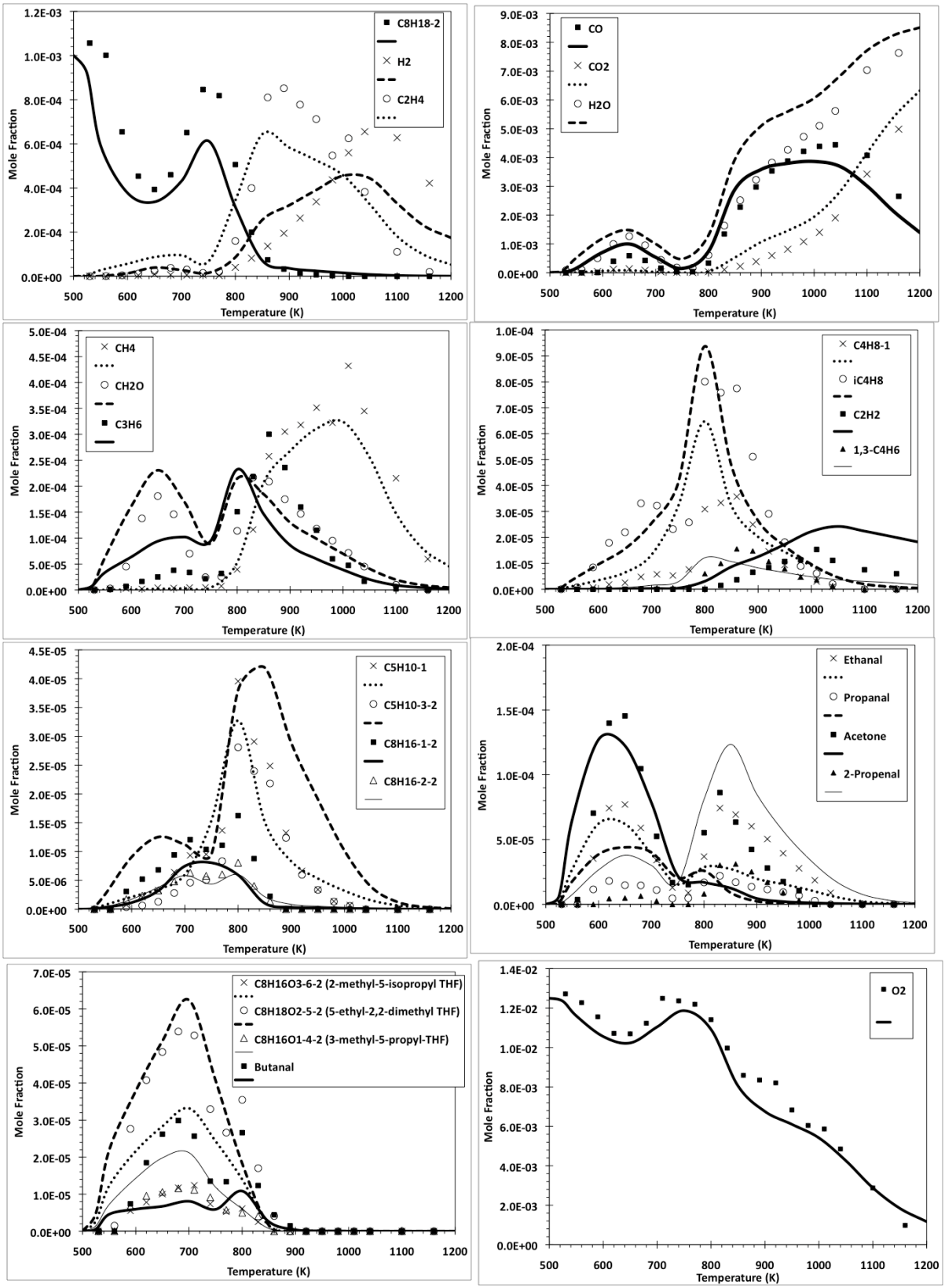

Figure 3 - 2-methylheptane oxidation in a JSR at 10 atm, τ = 0.7 s and ϕ = 1.0. The initial fuel (C_8H_{18}-2) mole fraction was 0.1%. Experimental data (symbols) are compared to calculations (lines with small symbols).

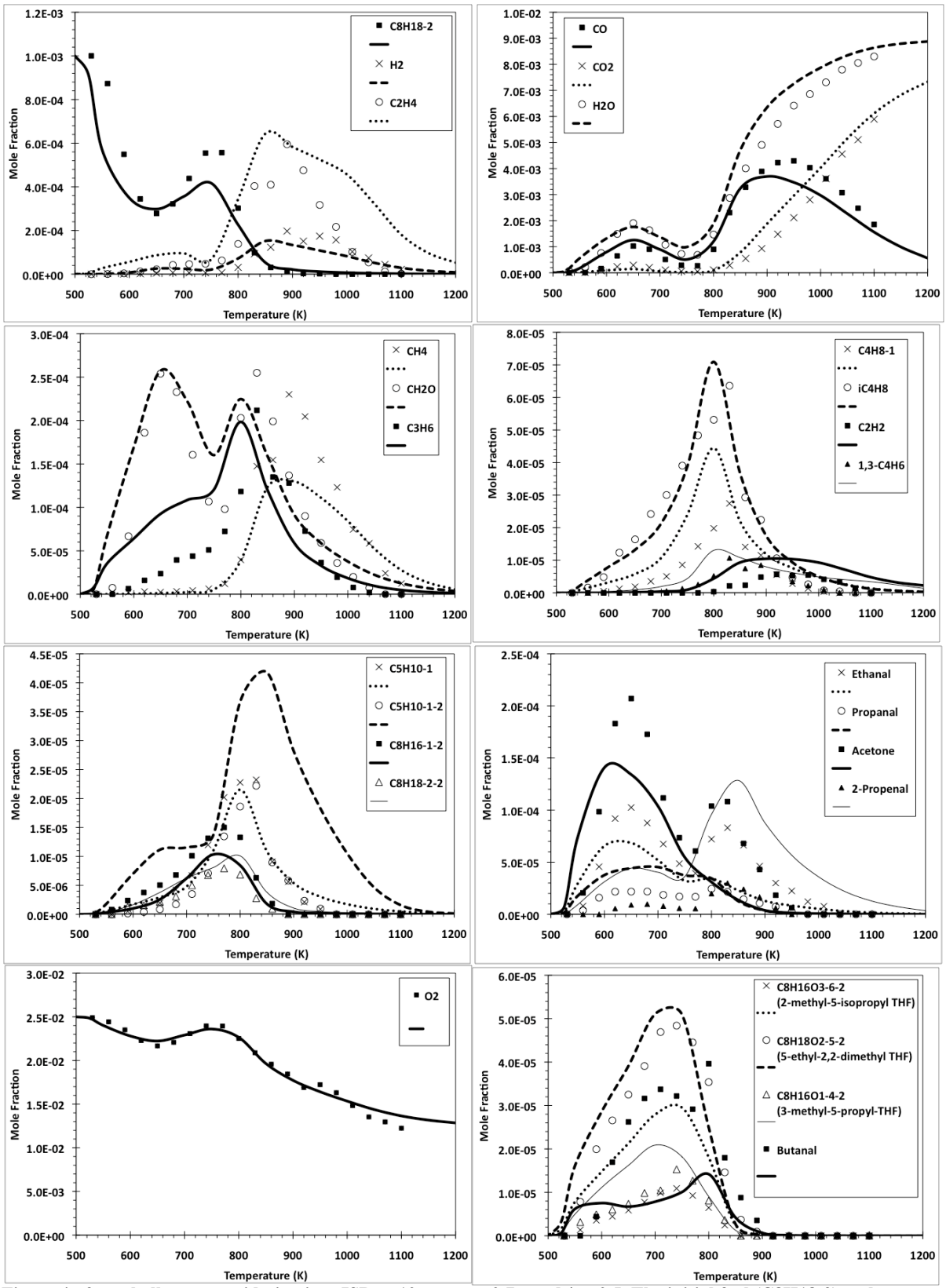

Figure 4 - 2-methylheptane oxidation in a JSR at 10 atm, τ = 0.7 s and ϕ = 0.5. The initial fuel (C8H18-2) mole fraction was 0.1%. Experimental data (symbols) are compared to calculations (lines with small symbols).

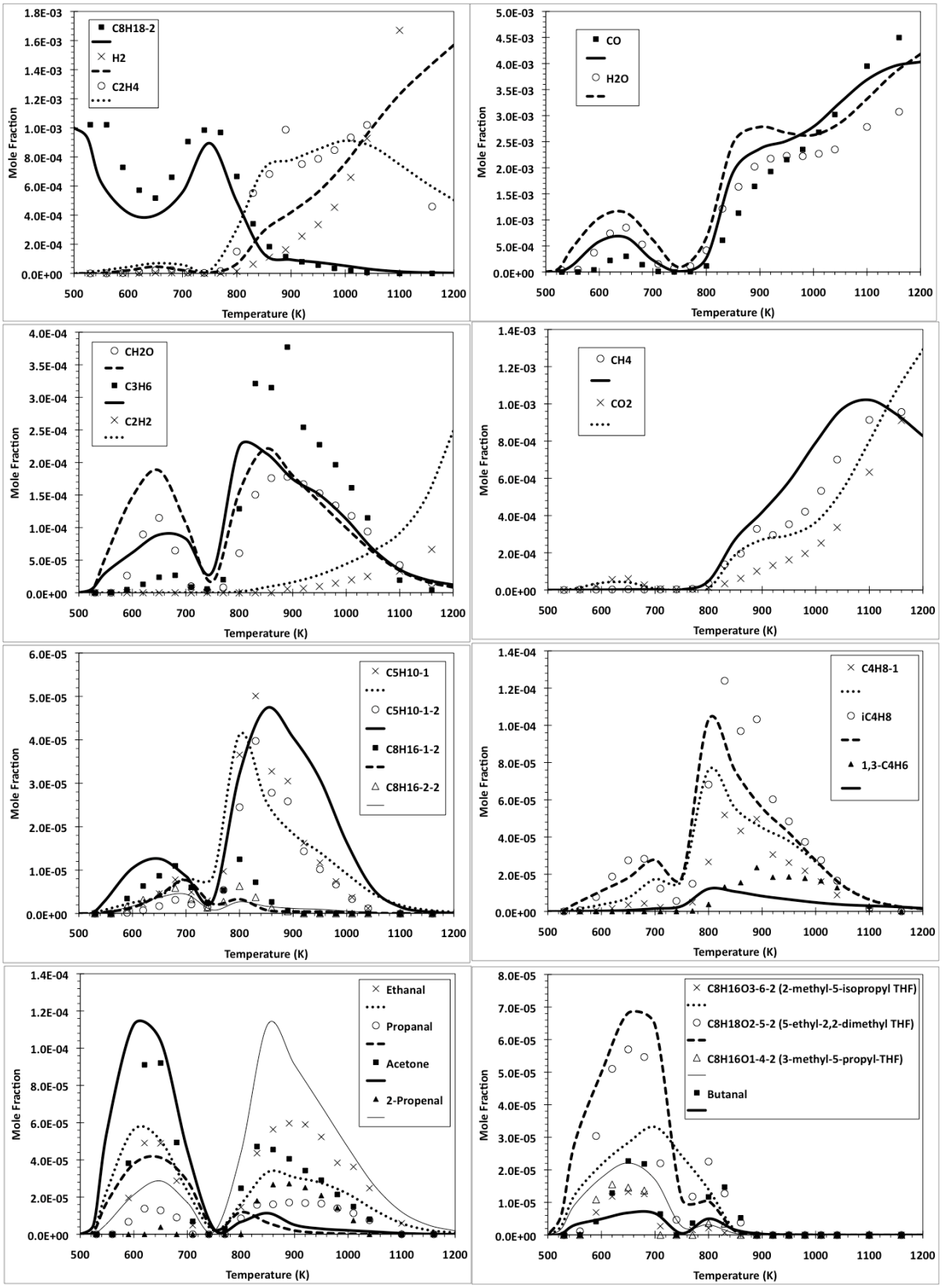

Figure 5 - 2-methylheptane oxidation in a JSR at 10 atm, τ = 0.7 s and ϕ = 2.0. The initial fuel (C_8H_{18}-2) mole fraction was 0.1%. Experimental data (symbols) are compared to calculations (lines with small symbols).

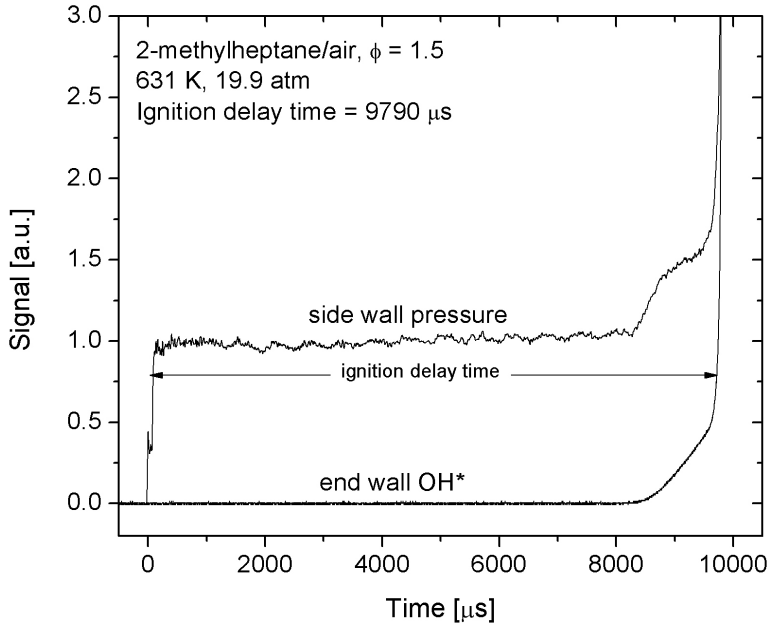

Figure 6 - Example ignition delay time measurement

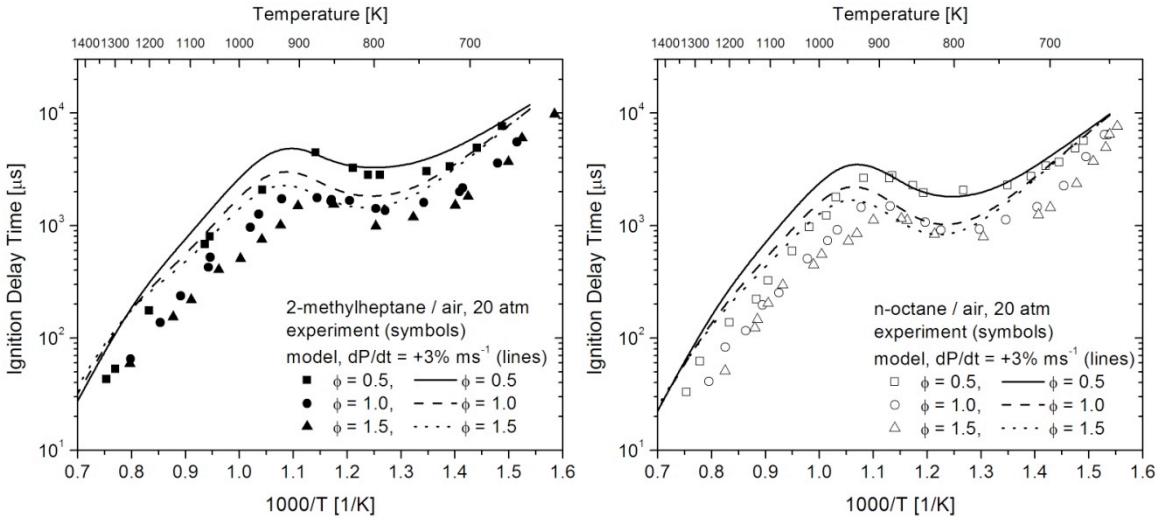

Figure 7 - Measured shock tube ignition delay times with comparison to kinetic modeling predictions: 2-methylheptane (left) and *n*-octane (right).

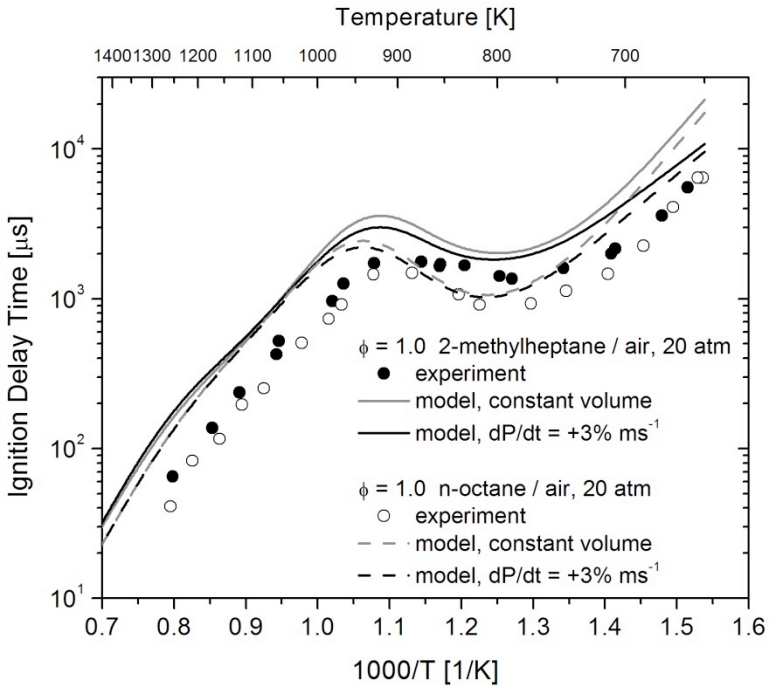

Figure 8 - Comparison of measured shock tube ignition delay times with kinetic modeling predictions for 2-methylheptane and *n*-octane at 20 atm, ϕ=3, in air. Kinetic modeling predictions are shown under the adiabatic constant volume constraint and for an imposed pressure rise rate of dP/dt = 3%/ms, as experimentally measured.

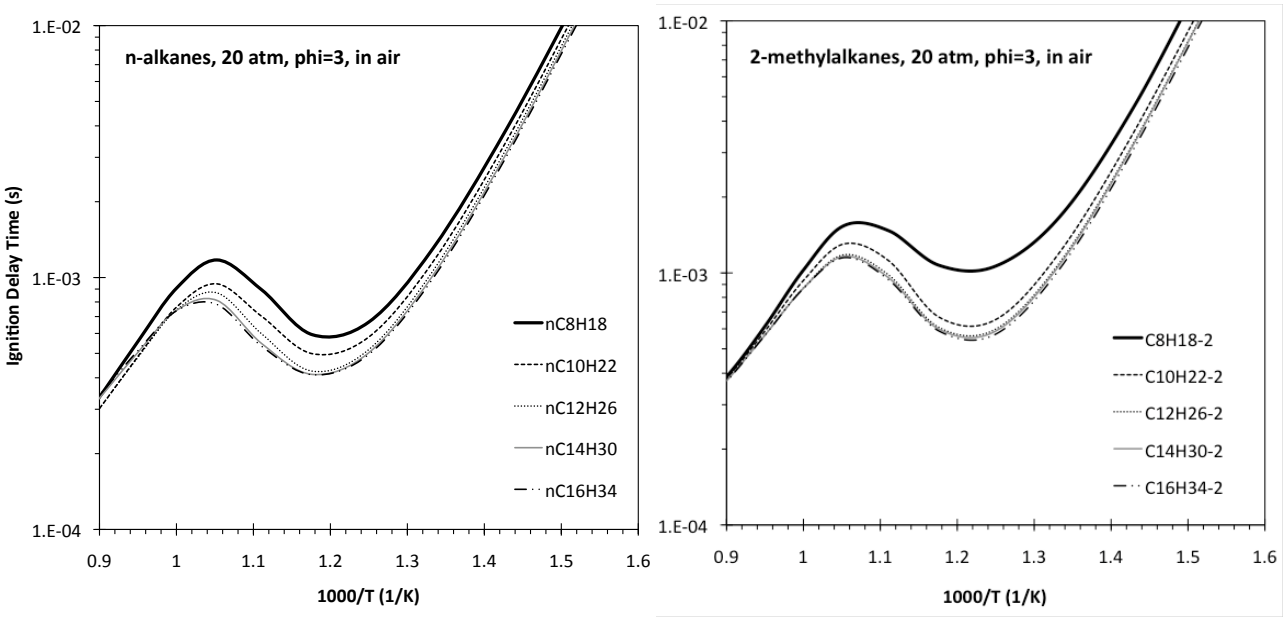

Figure 9 – Computed ignition delay times for even carbon number *n*-alkanes and *2*-methylalkanes from C_8 to C_{16} at 20 atm, ϕ=3, in air.

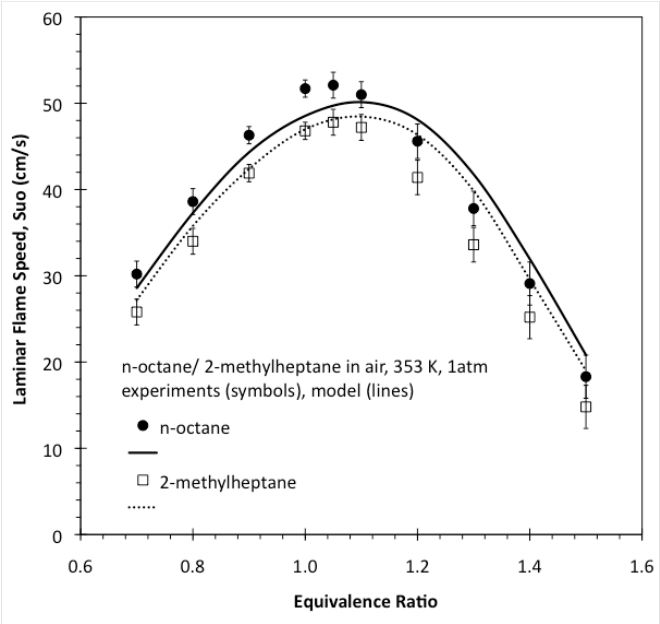

Figure 10 – Laminar flame speeds of *n*-octane (Ji et al. [53]) and 2-methylheptane in air at 353 K and 1 atm.

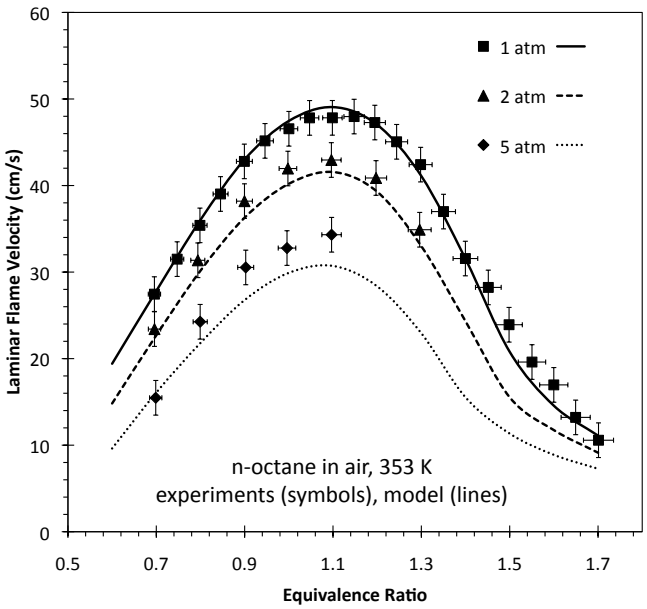

Figure 11 - Laminar flame speeds of *n*-octane (Kelley et al. [54]) at 353 K and various pressures.

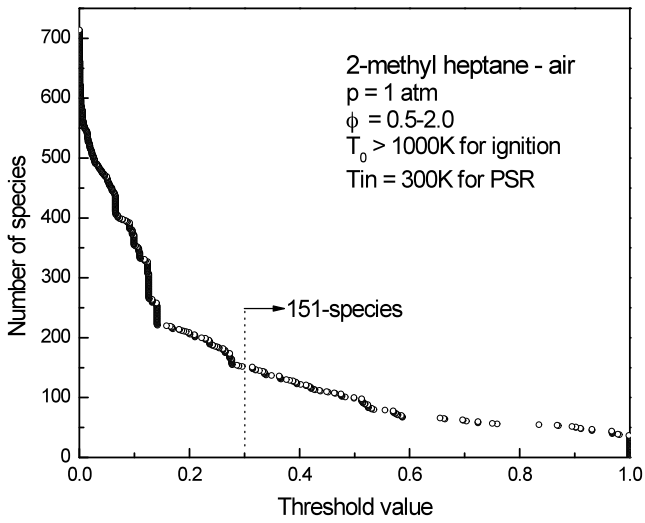

Figure 12 - The reduction curve of DRG using the definition in eq. (1) for *2*-methylheptane – air mixtures based on reactions states sampled from auto-ignition and PSR.

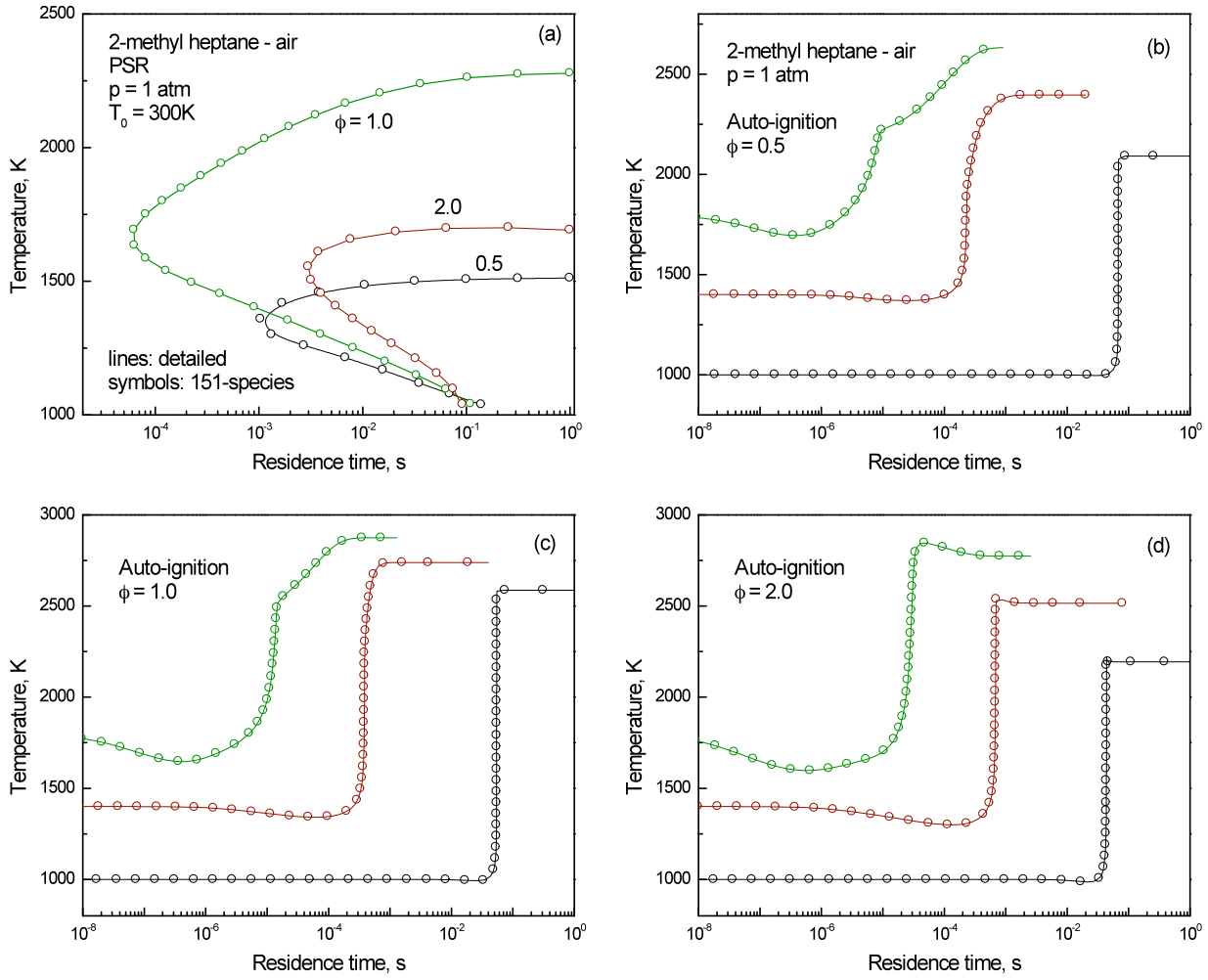

Figure 13 - Temperature as a function of the residence time calculated using the 151-species skeletal mechanism and the detailed mechanism, respectively, for *2*-methylheptane − air mixtures under atmospheric pressure for various equivalence ratios and fixed inlet temperature of 300K for PSR and different initial temperatures for auto-ignition.

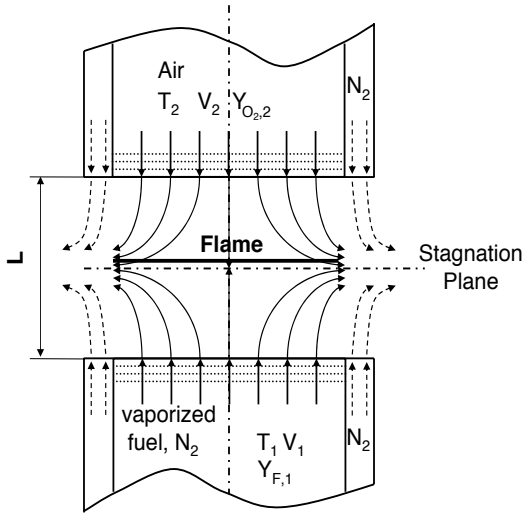

Figure 14 - Schematic illustration of the counterflow flow field

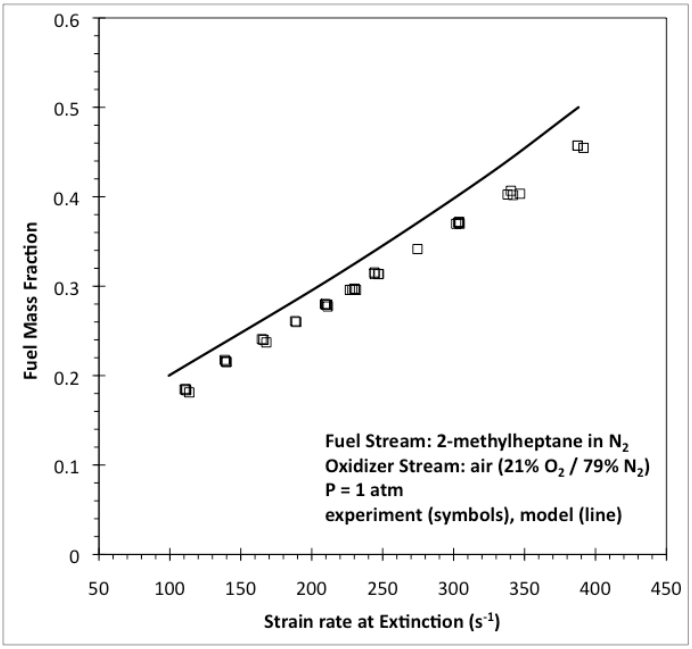

Figure 15 - The mass fraction of fuel, $Y_{F,1}$, as a function of the strain rate at extinction, $a_{2,e}$ in the counterflow flame. The symbols represent experimental data. The line is results of numerical calculation using the skeletal mechanism.

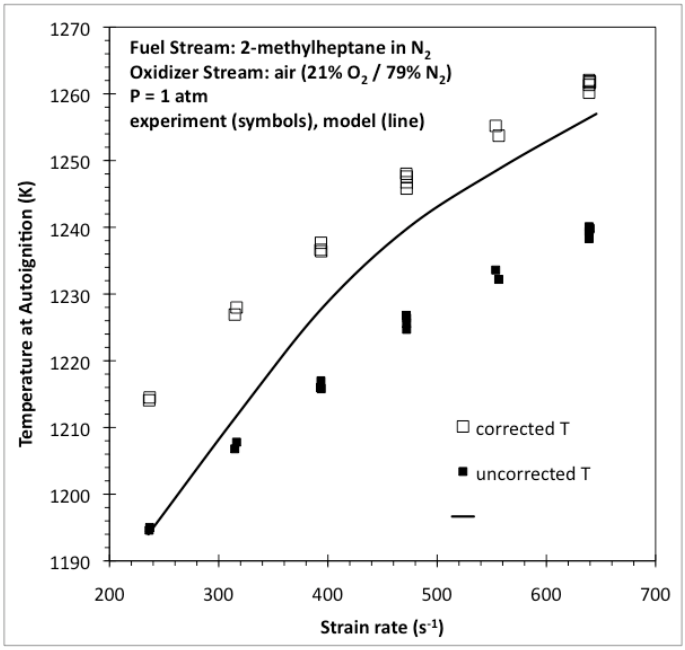

Figure 16 - The temperature of the oxidizer stream at ignition, $T_{2,I}$, as a function of the strain rate, a_2 for $Y_{F,I} = 0.4$ in the counterflow flame. The symbols represent experimental data. The line is result of numerical calculations using the skeletal mechanism.

8. Supplementary Material

Table 1. Reflected shock ignition delay time data for 2-methylheptane/air mixtures.

2-methylheptane/air, ϕ = 0.5: 0.833% 2-methylheptane, 20.83% O_2, and 78.33% N_2			2-methylheptane/air, ϕ = 1.0: 1.653% 2-methylheptane, 20.66% O_2, and 77.69% N_2			2-methylheptane/air, ϕ = 1.5: 2.459% 2-methylheptane, 20.49% O_2, and 77.05% N_2		
T_5 [K]	P_5 [atm]	τ [μs]	T_5 [K]	P_5 [atm]	τ [μs]	T_5 [K]	P_5 [atm]	τ [μs]
672	20.3	7626	660	21.0	5545	631	19.9	9790
694	19.1	4906	676	19.0	3583	656	20.7	6015
719	20.5	3352	707	19.5	2160	667	19.7	3693
742	20.3	3024	710	18.9	1998	702	18.1	1813
793	19.7	2813	745	20.3	1600	714	19.7	1511
807	22.5	2818	787	20.9	1359	756	19.3	1188
826	21.1	3253	798	21.5	1416	798	20.5	987
876	19.2	4461	830	20.6	1668	851	19.3	1537
959	21.8	2071	854	21.6	1707	902	18.7	1499
1058	21.8	797	855	21.3	1645	929	19.6	1008
1068	19.1	681	874	21.6	1771	960	20.6	752
1201	21.0	175	927	18.7	1726	998	21.1	509
1299	22.6	53	965	18.9	1261	1040	20.4	404
1327	21.7	43	980	21.4	965	1098	20.3	218
			1057	19.0	521	1140	20.0	154
			1061	20.1	425	1255	18.8	59
			1122	19.9	237			
			1172	20.7	137			
			1253	21.5	65			

Table 2. Reflected shock ignition delay time data for n-octane /air mixtures.

n-octane /air, $\phi = 0.5$: 0.833% n-octane, 20.83% O_2, and 78.33% N_2			n-octane /air, $\phi = 1.0$: 1.653% n-octane, 20.66% O_2, and 77.69% N_2			n-octane /air, $\phi = 1.5$: 2.459% n-octane, 20.49% O_2, and 77.05% N_2		
T_5 [K]	P_5 [atm]	τ [μs]	T_5 [K]	P_5 [atm]	τ [μs]	T_5 [K]	P_5 [atm]	τ [μs]
671	21.7	5669	651	22.1	6419	644	22.4	7620
678	21.1	4866	654	20.9	6413	650	21.1	6479
692	23.4	3660	669	22.7	4092	653	19.5	4948
704	21.5	3395	688	20.6	2261	663	20.5	3720
718	20.8	2728	712	20.2	1469	677	20.5	2357
741	20.3	2285	743	20.7	1127	700	20.1	1448
789	18.2	2056	771	20.1	931	711	18.2	1246
838	20.4	1951	816	21.0	912	767	19.5	795
852	19.6	2278	836	20.6	1072	824	19.2	839
881	18.7	2782	884	20.6	1489	860	19.4	1114
885	19.8	2630	928	20.9	1455	868	18.6	1153
924	20.6	2641	968	20.4	915	909	19.6	1119
970	20.2	1783	985	18.2	734	935	19.6	846
987	19.8	1226	1023	20.2	508	949	19.2	727
1019	18.6	967	1081	19.2	252	996	19.8	553
1053	21.7	590	1118	19.3	196	1011	18.7	448
1105	18.1	324	1158	19.4	116	1073	19.3	295
1132	22.0	220	1211	20.3	83	1105	20.6	203
1200	18.8	137	1258	22.7	41	1130	18.5	146
1285	20.1	62				1136	20.1	123
1327	19.6	33				1212	18.9	51